




RESEARCH ARTICLE OPEN ACCESS

High-Temperature Supercapacitors Enabled by Fluorine-Free Ionic Liquid and Synergistic Alkali-Doped Graphene Oxides

Gaurav Tatrari^{1,2}  | Tanmoy Rath³  | Klaudia Maślana^{4,5} | Rajesh Bhatt⁶ | Xuecheng Chen⁴  | Ewa Mijowska^{4,5} | Rong An⁵ | Solomon Tesfalidet¹ | Faiz Ullah Shah^{2,7}

¹Department of Chemistry, Umeå University, Umeå, Sweden | ²Chemistry of Interfaces, Luleå University of Technology, Luleå, Sweden | ³Department of Applied Sciences, Motihari College of Engineering (Bihar Engineering University), Motihari, Bihar, India | ⁴Department of Nanomaterials Physicochemistry, Faculty of Chemical Technology and Engineering, West Pomeranian University of Technology in Szczecin, Szczecin, Poland | ⁵School of Materials Science and Engineering, Herbert Gleiter Institute of Nanoscience, Nanjing University of Science and Technology, Nanjing, China | ⁶PRS-Nanoscience and Nanotechnology Centre, Department of Chemistry, D.S.B. Campus, Kumaun University, Nainital, Uttarakhand, India | ⁷Center for Advanced Materials and Manufacturing Process Engineering (CAMMPE), West Pomeranian University of Technology in Szczecin, Szczecin, Poland

Correspondence: Gaurav Tatrari (gaurav.tatrari@umu.se) | Faiz Ullah Shah (faiz.ullah@ltu.se)

Received: 9 June 2025 | **Revised:** 6 November 2025 | **Accepted:** 17 November 2025

Keywords: alkali metal doping | fluorine-free electrolytes | graphene oxide | ionic liquids | Supercapacitors

ABSTRACT

This study explores the synthesis and electrochemical performance of graphene oxide co-doped with sodium and potassium (Na–K–GO) as electrode materials for supercapacitors (SCs) designed to operate at 60°C over an extended voltage window. The Na–K–GO is employed as the electrode material, while a fluorine-free ionic liquid (IL), [P₄₄₄₄][MEEA]—comprising a tetrabutylphosphonium cation and a 2-2-(2-methoxyethoxy)ethoxy anion—served as the electrolyte, enabling stable operation over a wide voltage window at elevated temperatures. Using this combination, three coin-cell SCs are fabricated: two symmetric devices (SC-1 and SC-2) and one asymmetric device (SC-3). All the three exhibited remarkable charge storage abilities, a retaining performance over 10 000 charge–discharge cycles at 60°C. Among the three devices, SC-3 exhibited the best overall electrochemical performance, delivering a high specific capacitance of 47.01 F g⁻¹ and an energy density of 27.77 Wh kg⁻¹ at 0.5 A g⁻¹. Even at a higher current density of 1 A g⁻¹, SC-3 maintained a maximum power density of 1000 W kg⁻¹ while sustaining an energy density of 14.21 Wh kg⁻¹, reflecting its strong rate capability. Moreover, the long-term cycling tests at 2 A g⁻¹ demonstrated an outstanding durability of SC-3, which retained 99% coulombic efficiency after 10 000 cycles, significantly outperforming the SC-2 (90%) and SC-1 (79%).

1 | Introduction

Supercapacitors (SCs), or ultracapacitors, are advanced energy storage devices (ESDs) that bridge the gap between capacitors and rechargeable batteries. SCs combine the high power density and long cycle life of capacitors with the enhanced energy storage capacity of batteries, making them efficient and versatile candidates for next-generation ESDs [1, 2]. These advantages

make SCs attractive for applications ranging from wireless sensors and portable electronics to electric vehicles and grid-scale storage [2, 3]. Their performance depends strongly on electrode–electrolyte interactions, with the interface governing charge–discharge kinetics and overall stability [4, 5].

Consequently, the selection of highly efficient electrode materials is crucial for optimizing SC performance and maximizing

This is an open access article under the terms of the [Creative Commons Attribution](https://creativecommons.org/licenses/by/4.0/) License, which permits use, distribution and reproduction in any medium, provided the original work is properly cited.

© 2025 The Author(s). *Energy Storage* published by John Wiley & Sons Ltd.

interfacial charge storage. Among various candidates, graphene is a leading electrode material due to its exceptional conductivity (10^4 – 10^7 S cm $^{-1}$), high surface area (2630 m 2 g $^{-1}$), thermal conductivity (> 5000 W m $^{-1}$ K $^{-1}$), mechanical strength (~ 1 TPa), and optical transmittance ($> 97\%$) [6–11]. However, large-scale synthesis of high-quality graphene remains challenging, limiting practical applications. Graphene oxide (GO), a derivative rich in hydroxyl, epoxy, and carboxyl groups, provides a more accessible alternative [12, 13]. Although these functionalities lower conductivity (10^{-3} – 1 S cm $^{-1}$) [14–17], they enhance hydrophilicity, dispersibility, and reactivity, enabling surface functionalization. Reduction partially restores conductivity (1 – 10^4 S cm $^{-1}$) [18, 19], and GO's chemistry readily supports doping strategies to improve electrochemical performance [20, 21].

Alkali metal doping, particularly with sodium (Na) and potassium (K), has shown significant promise. Their high charge density and strong solvation effects enhance conductivity, increase active ion adsorption sites, and improve ion transport, thereby boosting capacitance and energy density [22, 23]. For example, pyrolyzed metal-doped GO with PVA–H $_3$ PO $_4$ gel electrolyte achieved 18.2 F g $^{-1}$ capacitance and 2.5 Wh kg $^{-1}$ energy density [24], while boron-doped graphene in 6 M KOH delivered 3.86 and 125 W kg $^{-1}$ [25]. Despite these advances, the energy density and capacitance of GO-based SCs remain limited. Aqueous electrolytes, though highly conductive, are constrained by a narrow voltage window (~ 1.2 V), leakage, and self-discharge [24–27]. Polymer electrolytes offer better stability but are hindered by low ionic conductivity, high interfacial resistance, and poor high-temperature performance [28, 29].

Ionic liquids (ILs) offer an attractive alternative, combining wide electrochemical windows, thermal stability, non-flammability, high ionic conductivity, and negligible vapor pressure [30–33]. They remain liquid below 100°C, resist crystallization, and maintain excellent stability [34, 35]. However, most ILs are fluorinated, raising toxicity and environmental concerns due to hazardous hydrolysis by-products such as HF [35, 36].

To address these challenges, fluorine-free ILs are being actively explored as sustainable alternatives with comparable electrochemical properties [37, 38]. For instance, pyrrolidinium- and morpholinium-based ILs with oligoether phosphate anions demonstrated high thermal stability, low T_g , and wide stability windows, enabling graphite SCs with 27 Wh kg $^{-1}$ energy density and 609 W kg $^{-1}$ power density at 90°C [38]. Similarly, a pyrrolidinium-based fluorine-free IL achieved 186 F g $^{-1}$ capacitance in symmetric graphite SCs [37]. Beyond environmental benefits, the absence of fluorine improves resistance to electrolyte breakdown and electrode passivation, extending device lifespan. Overall, fluorine-free IL electrolytes present a promising pathway to advance high-temperature SCs by combining wide-voltage operation, stability, and sustainability.

Here, we report a fluorine-free IL electrolyte composed of a tetrabutylphosphonium cation ([P $_{4444}$] $^+$) and a 2-[2-(2-methoxyethoxy)ethoxy]acetate anion ([MEEA] $^-$) (Figure 1). The presence of ether functionalities in [MEEA] $^-$ imparts structural flexibility, resulting in reduced viscosity, an extended electrochemical voltage window, and enhanced ionic

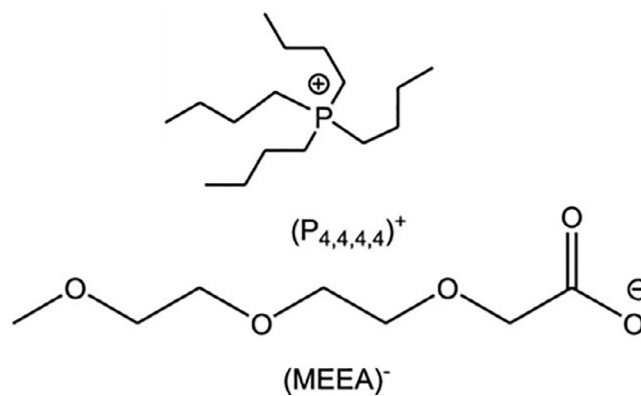


FIGURE 1 | Structure and abbreviation of the ionic liquid electrolyte investigated in this study.

conductivity over a wide temperature range [39]. These favorable transport properties and high electrochemical stability enabled its application as an electrolyte in SCs, employing different electrode configurations: symmetric devices (SC-1 with rGO electrodes and SC-2 with Na–K–GO electrodes) and an asymmetric device (SC-3 with rGO and Na–K–GO electrodes), all tested at 60°C. The Na–K co-doped GO electrode plays a critical role in advancing electrode design. Unlike single-alkali doping, the co-doping approach exploits the synergistic effect of Na $^+$ and K $^+$ ions, which differ in ionic radius and charge density. Their simultaneous incorporation optimizes defect distribution, enhances ion transport pathways, and enriches the surface chemistry, thereby creating additional active sites for charge storage.

Together, the integration of [P $_{4444}$][MEEA] as a sustainable fluorine-free electrolyte and co-doped GO as a high-performance electrode material demonstrates a promising route to expand the performance boundaries of SCs. This combined strategy enables wide-voltage operation, reliable high-temperature stability, and improved efficiency, offering significant potential for next-generation SCs.

2 | Experimental

2.1 | Materials

All commercial reagents were used as received without further purification. Graphite powder (ACS reagent, CAS No. 7782-42-5; particle size < 20 μ m), sodium nitrate (NaNO $_3$, ACS reagent, CAS No. 7631-99-4, $\geq 99\%$), concentrated sulfuric acid (H $_2$ SO $_4$, ACS reagent, CAS No. 7664-93-9, 95%–98%), potassium permanganate (KMnO $_4$, ACS reagent, CAS No. 7722-64-7), and hydrogen peroxide (H $_2$ O $_2$, ACS reagent, CAS No. 7722-84-1, 50 wt% in H $_2$ O, stabilized) were all procured from Sigma-Aldrich.

2-[2-(2-Methoxyethoxy)ethoxy]acetic acid (CAS No. 16024-58-1; MW 178.18 g mol $^{-1}$) and tetrabutylphosphonium hydroxide solution (40 wt% in water) were also obtained from Sigma-Aldrich. The ionic liquid [P $_{4444}$][MEEA] was synthesized by neutralizing tetrabutylphosphonium hydroxide with an equimolar amount of 2-[2-(2-methoxyethoxy)ethoxy]acetic acid. The mixture was stirred at room temperature for 4 h, and the water was removed by rotary evaporation under vacuum at an elevated temperature.

The product was further purified and dried under vacuum at 80°C for at least 24 h. The water content was verified to be <100 ppm by Karl Fischer titration (Metrohm 917 Coulometer, Switzerland), conducted in an argon-filled glovebox (H_2O and O_2 <1 ppm). Details of the synthesis and characterization of [P₄₄₄₄][MEEA] are available in our previous work [39].

Polyvinylidene fluoride (PVDF; CAS No. 24937-79-9) was purchased from Sigma–Aldrich, with a melt viscosity of 23.5–29.5 kP, a glass transition temperature of –38°C, and a melting point of 171°C. Activated carbon nanopowder (CAS No. 7440-44-0; coconut shell charcoal; Mesh Size: 60–70 nm; SSA > 1300 m² g⁻¹; electrical conductivity (0.4 Ω cm⁻¹); Purity ≥ 99.9%) was supplied by Nanografi and used as the electrode material.

2.2 | Synthesis of Graphene Oxide

The graphite was pretreated with dilute hydrochloric acid, followed by washing with distilled water. The carbon collected as GO was prepared with a modified Hummer method previously reported [6]. $NaNO_3$ (1.5 g) was mixed with H_2SO_4 and stirred for

30 min, keeping the temperature <20°C. Then, graphite powder (3 g) was added and stirred for 1 h at 200 rpm. Under vigorous agitation, $KMnO_4$ was gradually added, and the temperature was kept <20°C, followed by stirring for 30 min. After that, the mixture was transferred to 35°C and stirred for an additional 2 h at a speed of 800 rpm. Then, deionized water was added dropwise, causing a smoking effect and an increase in temperature. The dark green mixture was then diluted with deionized water and H_2O_2 .

After stirring for 1 h at 30°C, the mixture was precipitated for 24 h and centrifuged with hydrochloric acid (HCl) and water (1:10) at 4000 rpm for 10 min, and then washed with deionized water and ethanol until a pH = 7 was obtained to remove all the impurities. The mixture was filtered and heated at 80°C for 1 h. This step was repeated with the mass variation of graphite, and the ratio of graphite $NaNO_3$: $KMnO_4$ was kept constant (Figure 2) [6]. Furthermore, Na-K co-doped GO was synthesized using the same technique, with 1 g of each NaOH and KOH added to the GO solution and placed on a magnetic stirrer at 80°C for the following 8 h before being centrifuged. Additionally, the GO solution was converted to rGO using a hydrothermal reactor at

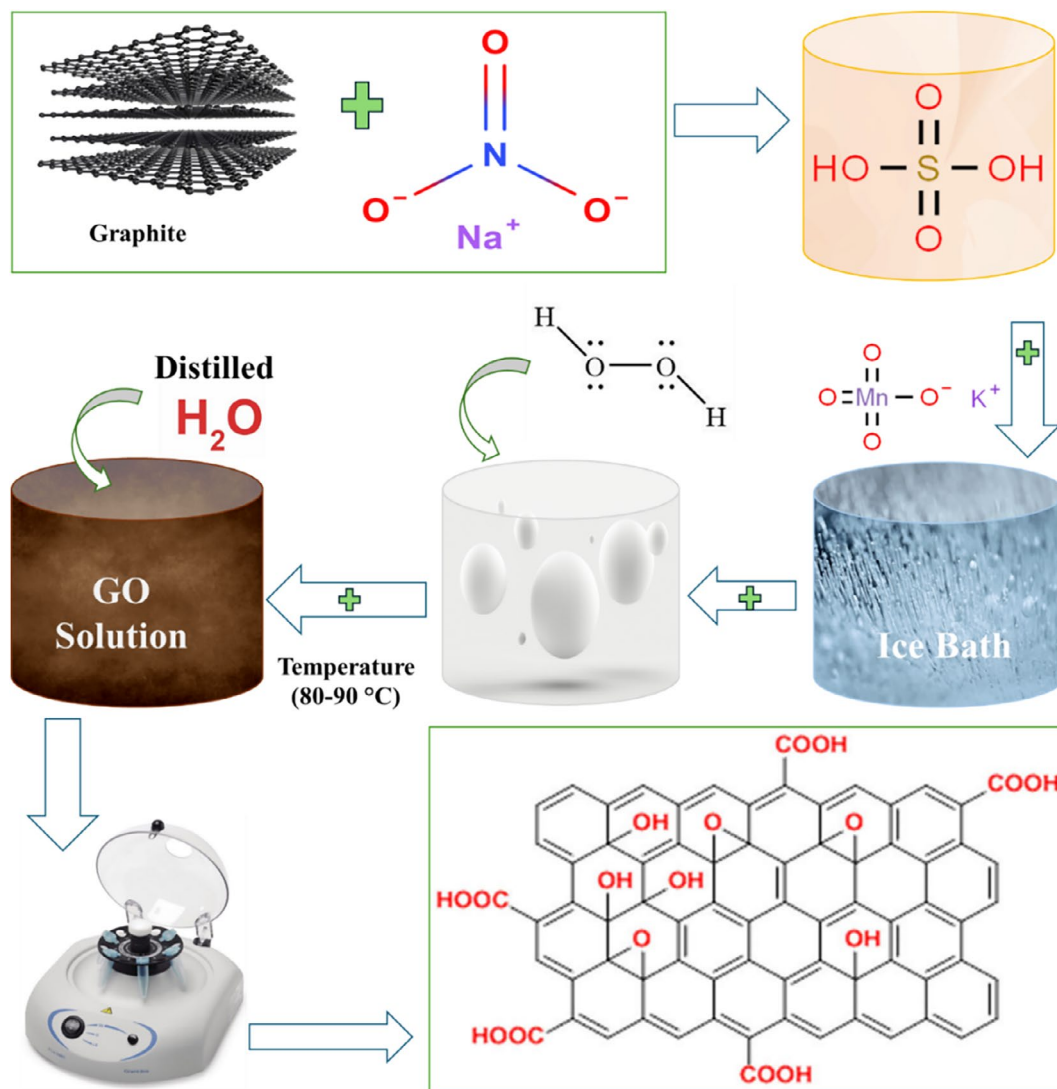


FIGURE 2 | Schematic illustration of GO synthesis via the modified Hummers' method.

160°C for 3 days in an oven before being used as an electrode material.

2.3 | Materials Characterization

The prepared GO and Na–K–GO samples were characterized using a range of advanced techniques to gain detailed insights into their structural and chemical properties. Raman spectroscopy (Horiba Japan Xplora Plus, 532nm excitation) was employed to identify the characteristic D and G peaks. X-ray diffraction (XRD) patterns were recorded using an Aeris diffractometer (Malvern Panalytical) with Cu–K α radiation to determine the crystalline structure and chemical composition. The internal morphology and structural features were further examined by transmission electron microscopy (TEM, FEI Tecnai G2 F20) operated at 200kV accelerating voltage.

Surface chemical composition and relative atomic percentages were analyzed by X-ray photoelectron spectroscopy (XPS) using Mg K α radiation ($h\nu = 1253.6\text{ eV}$) in a PREVAC system (Poland) equipped with a Scienta SES 2002 electron energy analyzer (Sweden), operated at constant transmission energy ($E_p = 50\text{ eV}$) under a base pressure below $5 \times 10^{-9}\text{ mbar}$. Scanning electron microscopy (SEM, Thermo Scientific Apreo 2S) was used to examine surface morphology, while energy-dispersive X-ray spectroscopy (EDX) was employed to determine elemental composition. Finally, the specific surface area and pore size distribution were evaluated using the Brunauer–Emmett–Teller (BET) method with N₂ sorption, following a preliminary degassing step (Figure S1).

2.4 | Electrode Preparation

The SC devices were fabricated by combining reduced GO, activated carbon (AC), and polyvinylidene fluoride (PVDF) binder in a 7:2:1 ratio. Initially, GO and AC were ground together using a mortar and pestle until a homogeneous powder was obtained.

Separately, 10wt% PVDF powder was dissolved in 4 mL of N-methyl-2-pyrrolidone (NMP) in a closed beaker at 60°C and stirred continuously for 4h. This PVDF solution was then added to the GO–AC mixture to form a uniform slurry, which was further mixed for 40 min and ground in a mortar and pestle to achieve a consistent texture. The resulting slurry was coated onto aluminum foil fixed to a glass substrate with ethanol, using a doctor blade set to 120 μm thickness to spread the slurry evenly across a $6 \times 6\text{ cm}^2$ area. Subsequently, coated sheets were calendered using a precision rolling press (ACEY-HRP100, Xiamen Acey New Energy Technology Co. Ltd.) at 40°C under 2–3 MPa for 2–3 min to ensure uniform electrode thickness. A similar procedure was used to prepare Na–K–GO electrodes on aluminum foil. All coated sheets were dried in a vacuum oven at 80°C for 2 days, after which electrodes with a diameter of 14mm were punched using an electrode cutter. The SCs were assembled by sandwiching a glass microfibre filter separator (18 mm, Whatman AFD grade) soaked in the IL electrolyte between two 14mm electrodes. This arrangement was clamped between glass slides and immersed in the IL electrolyte for 6 h at 60°C under reduced pressure to ensure

TABLE 1 | Cell architectures of the three SCs investigated in this study.

S. no	Cells structure
SC 1	GO Glass microfibre filter soaked with [P ₄₄₄₄][MEEA] GO
SC 2	K-Na-GO Glass microfibre filter soaked with [P ₄₄₄₄][MEEA] K-Na-GO
SC 3	K-Na-GO Glass microfibre filter soaked with [P ₄₄₄₄][MEEA] GO

thorough saturation of both separator and electrodes. Finally, coin cells (CR2032) were assembled and designated as SC-1, SC-2, or SC-3. All assembled cells were further dried in a vacuum oven at 60°C for 12h before electrochemical testing (Table 1).

2.5 | Device Characterization

The electrochemical performance of the fabricated devices was tested using Metrohm Autolab PGSTAT302N and Biologic BCS battery cycler. Cyclic voltammetry (CV) was employed to calculate the specific capacitance using a two-electrode system. The CV was performed using an IL electrolyte at various potentiometric parameters, including scan rates (1–100 mV s^{-1}), potential windows (0–2V), and stability cycles for all assembled SCs.

Electrochemical impedance spectroscopy (EIS) was carried out in the frequency range from 1 MHz to 0.01 Hz at 5mV amplitude, followed by 10cycles of CV at 50 mV s^{-1} using the Biologic BCS battery cycler. The CVs were interrupted by open circuit voltage (OCV) in between experiments to preserve accuracy in the potentiometric measurements.

Lastly, variable voltage (0.5–2V) CVs were performed for SC-3 with a scan rate of 50 mV s^{-1} to evaluate the stability of this system at different potentials. Moreover, the charge–discharge (CD) analysis of all the SCs was carried out at different current densities (1–2 A g^{-1}) over the potential window of 2V. Long-term CD experiments were carried out for 6000 and 10000 cycles for SC-2 and SC-3 using 2V. From CV tests, the specific capacitance (C_s) was calculated using Equation (1) [37, 38], and from GCD tests, it was calculated using Equation (2) [37, 38]; while the power and energy densities were evaluated for all the SCs using Equations (3) and (4), respectively [37, 38].

$$C_s = \frac{\int I dV}{2m K \Delta V} \quad (1)$$

$$C_s = \frac{I \Delta t}{m \Delta v} \quad (2)$$

C_s is the specific capacitance in Farads per gram, m is the mass in milligrams (1.5mg), K is the scan rate in millivolts per second, Δt is the discharge time in seconds, and ΔV is the potential window in volts. The energy density (E_D) and power density (P_D) were calculated using Equations (3) and (4) [37–41].

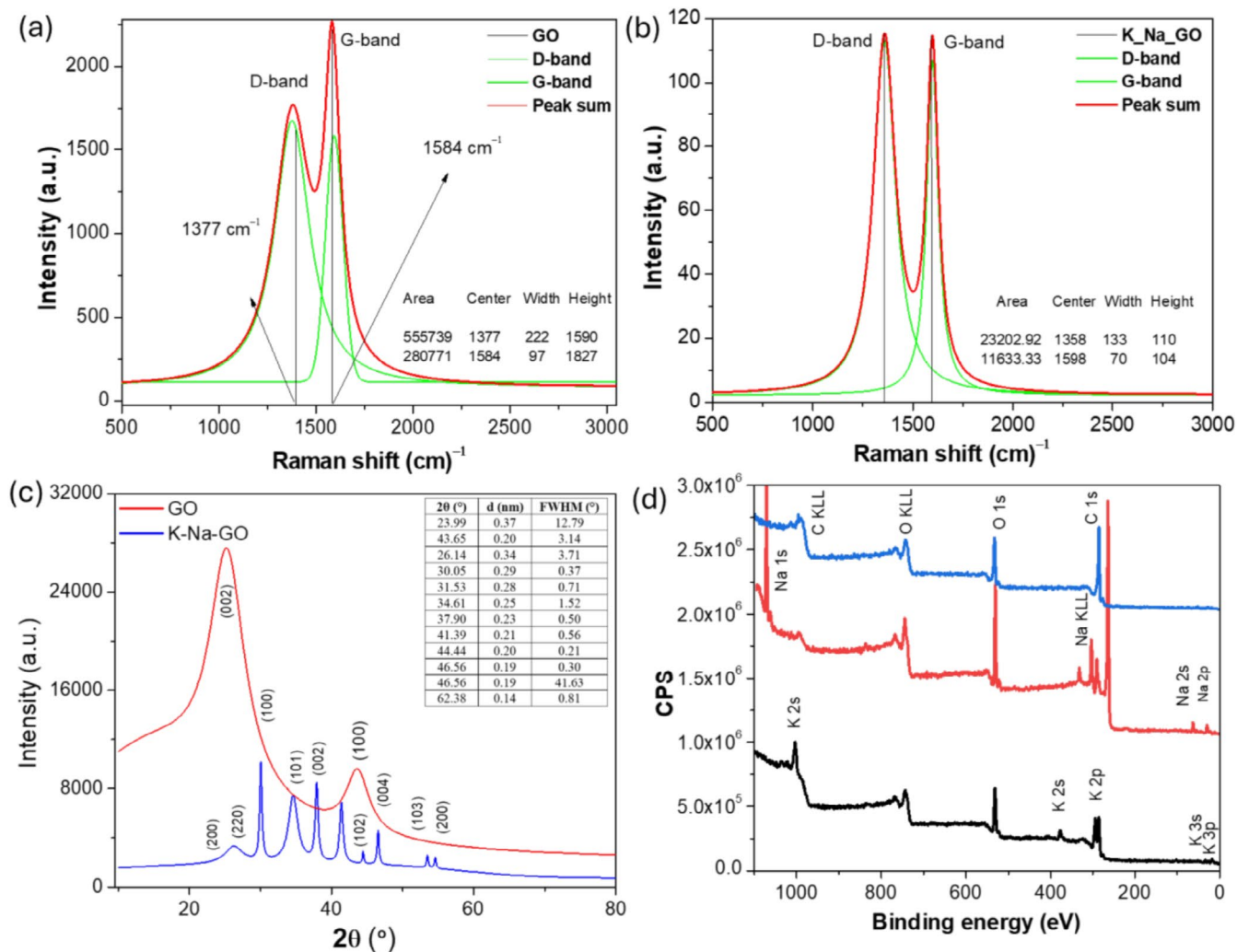


FIGURE 3 | (a) Raman spectrum of GO and its multi-peak fitting; (b) Raman spectrum of K-Na-GO with multi-peak fitting; (c) XRD patterns of GO and K-Na-GO; (d) XPS survey spectra of GO and K-Na-GO.

$$E_D = \frac{CV^2}{3.6 \times 2} \quad (3)$$

$$P_D = \frac{E_{D \times 3600}}{\Delta t} \quad (4)$$

3 | Results and Discussion

In the following sections, we begin with spectroscopic evaluation of the electrode materials, followed by morphological studies, and, finally, the systematic electrochemical assessments are discussed in detail.

3.1 | Spectroscopic Evaluation

Raman spectroscopy was employed to evaluate the structural characteristics of pristine GO and Na/K co-doped GO, using a Horiba Xplora Plus spectrometer with 532 nm excitation. For pristine GO, the D band appeared at $\approx 1377 \text{ cm}^{-1}$ with an area of 555739.2, a height of 1590, and a full width at half maximum (FWHM) of 222 cm^{-1} , while the G band was located at $\approx 1584 \text{ cm}^{-1}$ with an area of 280771.4, a height of 1827, and an

FWHM of 97 cm^{-1} . The intensity ratio was 0.87 (height-based) and 1.98 (area-based). Considering the broad nature of GO peaks, the area ratio is more reliable, yielding an $I_D/I_G \approx$ ratio of approximately 2.0. The in-plane crystallite size (L_a), estimated using the Cañado/Tuinstra-Koenig relation at 532 nm, was $\approx 9.7 \text{ nm}$. These values confirm a highly oxidized GO structure with abundant oxygen functionalities, broad defect distribution, and small sp^2 domains (Figure 3a) [42, 43]. For Na/K-GO, the D band was observed at $\approx 1358.8 \text{ cm}^{-1}$ with an area of 23202.9, a height of 110.8, and an FWHM of 133.3 cm^{-1} , while the G band appeared at $\approx 1598.2 \text{ cm}^{-1}$ with an area of 11633.3, a height of 104.4, and an FWHM of 70.9 cm^{-1} . The I_D/I_G ratio was 1.06 (height-based) and 1.99 (area-based), again confirming high defect density. The corresponding crystallite size was $\approx 9.6 \text{ nm}$, essentially the same as that of GO (Figure 3b) [41–44].

However, a key distinction is that the FWHM values for both the D and G bands in Na/K-GO were significantly narrower compared to pristine GO (D : 133 cm^{-1} vs. 222 cm^{-1} ; G : 71 cm^{-1} vs. 97 cm^{-1}). This narrowing suggests that co-doping promotes modest improvements in ordering and domain uniformity, even though the overall defect density remains high. While the total

defect density (I_D/I_G and L_a) remains similar to that of pristine GO, the redistribution and partial reorganization of defects lead to sharper band profiles and slightly enhanced structural uniformity.

This implies that Na⁺ and K⁺ ions, owing to their distinct ionic radii and charge densities, synergistically influence defect sites and interlayer spacing [41–44]. Such modifications are expected to improve ion transport and electronic conductivity while retaining a high density of active sites for charge storage. This structural interplay—retention of abundant defects with enhanced uniformity—provides an ideal balance for SC applications, offering both active sites for ion adsorption and sufficient graphitic pathways for efficient charge transport [41–44].

Furthermore, the XRD pattern of GO obtained from Lorentzian fitting shows two characteristic reflections (Figure 3c). The first and most intense peak appears at $2\theta = 23.99^\circ$, corresponding to an interlayer spacing of 0.37 nm with a very broad FWHM of 12.79° assigned to a collapsed graphitic (002)-like band. Instead of the typical hydrated GO (001) peak near 10° – 12° ($d \approx 0.8$ nm), this broad feature confirms that the interlayer distance has contracted toward graphite-like spacing due to dehydration and partial deoxygenation, leading to turbostratic restacking of the sheets [43–45]. A second, weaker reflection is observed at $2\theta = 43.65^\circ$ ($d = 0.20$ nm, FWHM = 3.14°), which corresponds to the (100)/(101) in-plane planes of graphitic domains. The relative intensity ratio ($A_2/A_1 \approx 0.06$) confirms that out-of-plane stacking dominates, while in-plane crystallinity is limited. The strong broadening of the $\sim 24^\circ$ band indicates small stacking coherence (~ 0.63 nm, ~ 2 layers) and significant disorder, consistent with partially reduced or anhydrous GO, while the weak 43.6° reflection points to the partial restoration of short-range sp^2 domains [43–45].

In contrast, the XRD profile of K–Na modified GO reveals a markedly different pattern with multiple sharp reflections (Figure 3c). A broad but distinct peak at $2\theta = 26.14^\circ$ ($d \approx 0.34$ nm, FWHM = 3.71°) can be regarded as a shifted (001)-like reflection, suggesting partial retention of an expanded interlayer spacing compared with graphite [6, 12, 24]. Several sharper peaks are then observed between 30° and 48° , with d -spacings ranging from 0.29 to 0.19 nm. Among them, the reflection at 30.05° ($d = 0.29$ nm, FWHM = 0.37°) indicates crystalline ordering, while a secondary peak at 31.53° ($d = 0.28$ nm) corresponds to a minor crystalline phase [43–45]. The strong peaks at 34.61° , 37.90° , and 41.39° ($d = 0.25$ – 0.21 nm) can be attributed to partially restored graphitic domains as well as alkali-derived crystalline phases, with the 41.39° reflection matching the (100)/(101) planes of graphitic carbon, indicating enhanced in-plane sp^2 ordering. Additional weaker peaks at 44.44° and 46.56° ($d = 0.20$ – 0.19 nm) also confirm the presence of crystalline components, while an extensive component at the same 46.56° position (FWHM $\approx 41.6^\circ$) reflects background or amorphous scattering.

Finally, a high-angle reflection at 62.38° ($d = 0.14$ nm) further supports the formation of crystalline domains [43–45]. Collectively, these results demonstrate that K–Na treatment eliminates the hydrated GO (001) reflection near 11° , collapses and reorganizes the interlayer galleries, and transforms GO

from a turbostratic, highly disordered material into a multiphase composite with both restored graphitic order and alkali-derived crystalline phases (Table S1). The XRD results complement the Raman analysis, together confirming that alkali incorporation reduces oxygen functionalities.

This is evidenced by the diminished D-band intensity in Raman spectra and the simultaneous emergence of sharp crystalline peaks in XRD, both of which indicate structural reorganization into a more ordered, multiphase composite [45, 46]. This behavior can be attributed to interactions between the carboxyl and ketone groups of GO with Na/K ions, which enhance bond stretching and lower bond decomposition energy, thereby facilitating structural reorganization into a multiphase crystalline composite [12, 24].

The XPS survey of GO shows only carbon and oxygen, with core-level peaks at $C_{1s} = 285.417$ eV and $O_{1s} = 532.417$ eV, confirming the expected composition (Figure 3d) [6, 12, 47, 48]. Deconvolution of the C_{1s} region (Figure 4a,b) is dominated by the sp^2/sp^3 C–C/C–H component centered near ~ 285 eV (consistent with the measured 285.417 eV; literature sometimes cites ~ 284.8 – 285 eV).

While the O_{1s} envelope is broad (~ 527 – 534 eV) and attributable to C–O (epoxy/hydroxyl), C=O, and adsorbed H_2O contributions. Overall, the survey quantification gives C = 81.1% and O = 18.9% for GO (O/C ≈ 0.23), verifying the successful synthesis of GO with carbon and oxygen as the sole detectable elements.

In the K–Na–GO composite, the survey scan evidences alkali incorporation alongside C_{1s} and O_{1s} , showing the characteristic K_{2p} doublet ($2p_{3/2} \sim 293.4$ eV, $2p_{1/2} \sim 296$ eV), $K_{2s} \sim 378$ eV, $Na_{2p} \sim 31$ – 33 eV, $Na_{2s} \sim 63$ eV, and $Na_{1s} \sim 1073$ – 1085 eV (Figure 4c–f) [6, 46–48]. These core levels confirm the presence of Na and K and indicate bonding environments that include Na/K–oxygen species (e.g., oxides/hydroxides/carbonates) together with the carbon framework. For pristine GO, C_{1s} (285.42 eV) and O_{1s} (532.42 eV) peaks with an O/C ratio of ~ 0.23 were observed. Deconvolution of C_{1s} revealed dominant sp^2/sp^3 C–C (~ 285 eV) and oxygenated components (C–O, C=O, O–C=O). After modification, the composite exhibits additional Na_{1s} (1073–1085 eV) and K_{2p} (293.4 and 296 eV) peaks, confirming successful Na/K doping. The atomic composition shifts to C = 44.8%, O = 27.1%, Na = 17.2%, K = 12.9% (Na:K ≈ 1.33 :1), with a higher apparent O/C ratio (~ 0.61) due to oxygen bound to alkali phases (Table 2).

The C_{1s} spectra reveal an increase in the sp^2 carbon component accompanied by a slight negative binding energy shift (-0.25 eV), indicating n-type doping and charge transfer from Na and K ions to the carbon framework. This behavior is consistent with partial deoxygenation and the restoration of conjugated π -domains. The resulting structural reorganization leads to enhanced electrical conductivity, attributed to stronger π – π conjugation, a reduction in oxygen-related defect sites, and improved crystallinity. The combined XPS and XRD analyses thus offer a clear quantitative and mechanistic picture of how Na/K incorporation modulates defect density, electronic structure, and charge transport within the composite. Moreover, the higher O/C ratio observed for the Na–K–GO composite (0.61 vs. 0.23

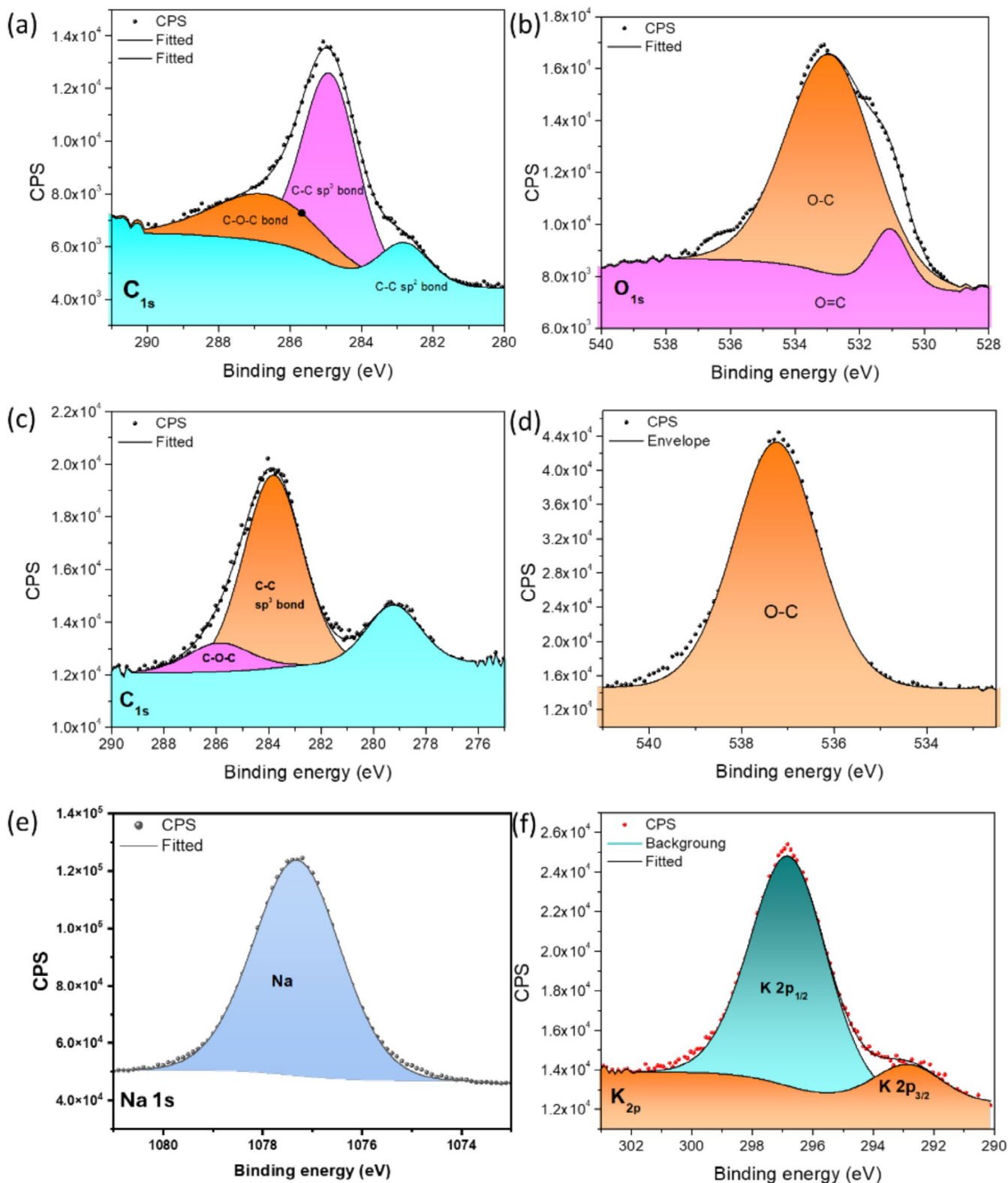


FIGURE 4 | XPS spectra of GO; (a) C_{1s} and (b) O_{1s}, and XPS spectra of the composite material; (c) C_{1s}; (d) O_{1s}; (e) Na_{1s}; (f) K_{2p}.

for GO) primarily arises from oxygen bound to alkali-derived phases and the relative decrease in carbon content, rather than from increased surface oxidation. This finding aligns with the Raman and XRD evidence, confirming effective alkali-induced structural reorganization of GO into a more ordered, conductive framework.

Brunauer–Emmett–Teller (BET) analysis, based on N₂ physisorption, shows that pristine GO has a specific surface area of 22 m²g⁻¹, which decreases for the K–Na–GO composite (Figure S1). The drop in area is consistent with restacking/compaction of GO sheets and partial pore blocking by Na⁺/K⁺ containing phases formed during modification. Raman and

TABLE 2 | The atomic surface composition of both samples was determined from XPS.

Element	GO (%)	Na-K-GO (%)
C _{1s}	81.1	44.8
O _{1s}	18.9	27.1
K _{2p}	0	12.9
Na _{1s}	0	17.2

XRD further validate the synthesis of both materials: GO displays a broad, collapsed (002)-like band near $\sim 24^\circ$ and a weak (100)/(101) feature, while K-Na-GO shows multiple sharp reflections between $\sim 30^\circ$ and 48° , evidencing the emergence of crystalline domains and alkali-derived phases. Overall, BET, XRD (restacking and new crystalline peaks), Raman (graphitic re-organization), and XPS (Na/K incorporation and altered elemental ratios) tell a consistent story: alkali treatment reorganizes the GO structure, yielding a multidimensional composite.

3.2 | Morphological Evaluation

SEM imaging of the same material across multiple magnifications (Figure 5a-h; 5–30 μm) reveals the expected lamellar GO scaffold—stacked, exfoliated sheets with gentle wrinkling and terracing—over which Na/Na/K-derived crystallites are uniformly distributed. In low-mag views, the surface appears stratified and continuous; higher-mag panels resolve bright, needle-like and dotted deposits decorating sheet faces, edges, and interlayer galleries, producing a characteristic “flower-like” motif against the diffuse GO background. To quantify these textures, ImageJ segmentation (5 μm calibration; conservative global threshold 100–255 with a size floor ≥ 0.05 –0.1 μm^2 ; edge objects excluded) gives a sharp contrast between the GO field and the K/Na-GO field. For GO, only 8 flakes are resolved, totaling 89.86 μm^2 —about 17.9% of a $\sim 502 \mu\text{m}^2$ field. Flakes are firmly micron-scale: Feret (max caliper) spans 3.68–13.28 μm (median $\approx 4.70 \mu\text{m}$; mean $\approx 5.66 \mu\text{m}$), the average perimeter is 11.83 μm , and areas yield an ECD distribution of D10/D50/D90 $\approx 2.94/3.60/4.37 \mu\text{m}$ (mean ECD $\approx 3.71 \mu\text{m}$). Shapes are compact and largely convex (circularity ≈ 0.922 ; solidity ≈ 0.97), and the mean Feret angle ($\sim 131^\circ$) indicates no preferred in-plane orientation; the number density is low (~ 0.016 flakes μm^{-2} ; $\sim 1.6 \times 10^4$ flakes mm^{-2}).

In contrast, the K/Na-GO image contains 182 flakes totaling 33.48 μm^2 (coverage $\approx 1.67\%$) over an estimated $\sim 1998 \mu\text{m}^2$ field. Sizes are predominantly sub-micron (Feret mean: 0.59 μm ; median: 0.509 μm ; IQR: 0.32–0.87 μm ; range: 0.04–2.71 μm), with perimeter averaging 1.713 μm and scaling strongly with Feret ($r \approx 0.98$). While particles are still mostly compact, they are notably more irregular than GO (circularity mean 0.684, SD ~ 0.18 ; $\sim 41\%$ with circularity ≤ 0.6), and solidity from the slice summary (0.845) points to edge roughness/minor voids or overlaps; the number density is correspondingly higher (~ 0.091 flakes μm^{-2} ; $\sim 9.1 \times 10^4$ flakes mm^{-2}). Taken together, the SEM textures and the image analysis indicate that Na/K modification transforms

a few large, compact GO sheets (high coverage, micron-scale Feret) into many smaller, sub-micron fragments with lower coverage, higher number density, and more irregular outlines—consistent with alkali-induced etching/fragmentation and the homogeneous dispersion of Na/K phases within and between GO layers (Figure 5a-h; 5–30 μm).

TEM analysis was carried out to investigate the internal structure of both pristine GO and K-Na functionalized GO (Figure 6). TEM images of GO acquired at different magnifications (50, 100, 200, and 500 nm) reveal the sheet-like morphology with characteristic internal stacking. At higher resolution (5 nm), layered stacking within selected regions is clearly visible (Figure 6a,b). Figure 6c highlights separated stacks in three distinct sheet regions, while Figure 6d shows diffuse stacking within the planar structure, confirming the sheet-like nature observed in SEM images. TEM analysis of GO and K-Na-GO consistently reveals diffuse features characteristic of disordered or turbostratic structures. In the 50 nm GO image, FFT analysis of a 512×512 px high-variance ROI calibrated from the 10 nm scale bar (0.035 nm px⁻¹, FOV ≈ 68.6 nm) shows a broad halo without discrete spots or rings.

The corresponding radial power spectrum lacks peaks at the graphitic (002) (~ 0.34 nm) and (100) (~ 0.21 nm) spacings, instead displaying broad features at larger *d*-spacings (~ 1.76 , 1.29, 0.78, 0.60, 0.27, and 0.19 nm), indicative of an amorphous or turbostratic phase with weak periodicity. K-Na functionalized GO at 50 nm magnification shows a similar diffuse halo and absence of graphitic peaks, with additional broad intensity bands (~ 2.7 , 1.02, 0.80, 0.64, 0.52, 0.45, and 0.38 nm), suggesting that alkali incorporation perturbs interlayer registry and further broadens local spacings. At 100 nm magnification, the material again displays no distinct lattice fringes, and FFTs remain diffuse, with radial spectra dominated by broad bands at $d \approx 0.38$ –2.7 nm.

Comparative analysis across the 10, 50, 100, 200, and 500 nm images confirms the sharp diffraction features at the expected graphitic frequencies, but the material lacks long-range crystalline order. ROI-based scans with ring guides spectra indicate that graphitic domains are present but poorly oriented (Figure 6a-h). Overall, both pristine GO and K-Na functionalized GO exhibit predominantly amorphous/turbostratic character, with short-range order limited to broadened bands at larger interplanar spacings. TEM images of the composite at 50–500 nm further highlight the effect of K and Na functionalization (Figure 6e-h).

Figure 6e reveals widely distributed diffuse rings, characteristic of a partially crystalline composite, while Figure 6f shows planar internal regions with bubble-like features attributed to extensive linkage of GO with alkali ions. Intensity profile analysis of gray value versus distance indicates a decreasing contrast, consistent with structural deformation of the graphene layers and partial enhancement in layer separation or closure upon K and Na incorporation (Figure 6g,h). The interior surface morphology (Figure 6h) is irregularly distributed, reflecting directed orientation and localized perturbations. Spherical features are visible on the GO sheets, with dark contrast regions and lines corresponding to potassium and sodium decoration on the surface.

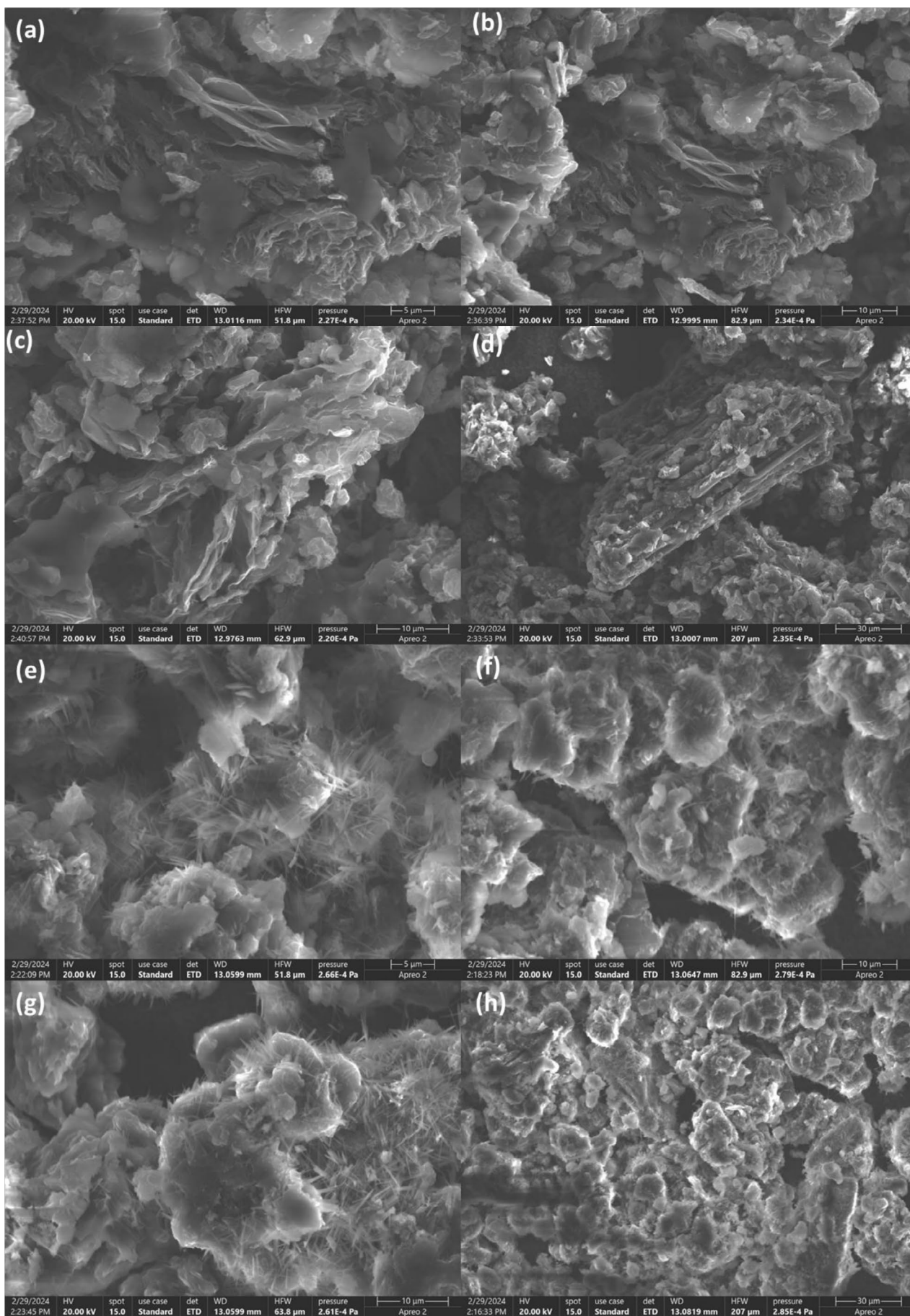


FIGURE 5 | Legend on next page.

FIGURE 5 | SEM images of GO: (a) 5 μm ; (b) 10 μm ; (c) 10 μm ; (d) 30 μm . SEM images of composite material: (e) 5 μm ; (f) 10 μm ; (g) 10 μm ; (h) 30 μm .

3.3 | Electrochemical Evaluation

GO has previously been examined as an electrode material due to its higher electric conductivity and electrolyte accessibility; nevertheless, all investigations have mostly focused on aqueous and fluorinated electrolytes. Besides, there is no study on fluorine-free IL electrolytes with GO and the effects of alkali metals on the electrochemical performance of the GO in SCs. To investigate the effects of K and Na doping on GO, the electrochemical performance of both materials (GO and K–Na–GO) as electrode materials was assessed using a fluorine-free ionic liquid electrolyte, $[\text{P}_{4444}][\text{MEEA}]$.

Generally, phosphonium-based ILs have high thermal stability ($> 300^\circ\text{C}$), an extended liquid temperature range, and are suitable as temperature-stable electrolytes for SCs [37–39]. Additionally, our previous research has demonstrated that the systems have a glass transition temperature of -80°C , attributed to the ethoxy units present in the anionic counterparts of the IL. This property enables low-energy rotations, rendering the IL an ideal electrolyte for both high- and low-temperature SC investigations [37]. The $[\text{P}_{4444}][\text{MEEA}]$ IL electrochemical stability window is over 4 V [37–39].

The CV analysis of SC-1, SC-2, and SC-3 performed at 60°C using different scan rates and potential windows is presented in Figure 7. At low scan rates for SC-1 ($1\text{--}10\text{ mVs}^{-1}$), the voltammogram of the CV is rectangular and less distorted, indicating a stronger capacitive behavior of the capacitor (Figure 7a). However, at high scan rates ($50\text{--}100\text{ mVs}^{-1}$), the voltammograms show a weaker capacitive behavior of SC-1 (Figures 7a and S3a,b). The transition from a predominantly rectangular pattern in the CVs to a more diffuse structure at higher potential scan rates suggests that the electrode materials based on GO do not possess high conductivity and structural alignment, resulting in limited porosity and surface area.

As a result, the SC-1 does not exhibit improved CV profiles at fast charging and discharging rates, even at a higher temperature of 60°C . In addition, the examination of particular capacitance shows a drop in capacitance for the SC-1 as the scan rates increase (Figure 7a). However, in the case of SC-2, the presence of metal ions in the GO structure distorts the CV profile of the device, moving from a low to a higher scan rate. This distortion is more pronounced in SC-2 compared to SC-1, although SC-2 exhibits a higher CV absolute area, which displays overall better capacitance performance (Figure 7b). This demonstrates that doping the GO with alkali metal ions improves capacitive performance; the insertion of these dopants brings electrons into the GO structure. After doping, the samples are thermally reduced [49, 50]. This procedure eliminates numerous oxygen functional groups, lowering the sheet resistance of GO and increasing its electrical conductivity and capacitance profile of the material [49, 50]. The highest specific capacitances of 83 Fg^{-1} were reported for SC-1, lower than SC-2, with 119 Fg^{-1} at 1 mVs^{-1} over

a potential window of 2 V at 60°C . However, upon increasing the scan rates, both SC-1 and SC-2 exhibited relatively low capacitance performance.

Specifically, SC-2 had a greater capacitance of 19 Fg^{-1} compared to SC-1, which had a capacitance of 8 Fg^{-1} , both measured at a scan rate of 100 mVs^{-1} over a potential of 2 V at 60°C . The SC-3 exhibited a greater capacitance of 163 Fg^{-1} as compared to SC-1 and SC-2 when tested at a scan rate of 1 mVs^{-1} and a voltage of 2 V at a temperature of 60°C . Furthermore, when the scan rates were increased, SC-3 exhibited a much greater capacitance of 28 Fg^{-1} , surpassing the capacitance of SC-1 and SC-2 at a scan rate of 100 mVs^{-1} (Figures 7c,d and S3). The results indicate that SC-3 has a greater specific capacitance than coin cells with GO and composite-based symmetric SCs at all scan speeds (Table S2). This demonstrates the superior potential of composite materials with asymmetric cell structure.

In addition, the enhanced performance at elevated temperatures may be attributed to the flexible structure of the carboxylate anion, composed of straight-chain ethoxy ether, leading to a lower viscosity and increased ionic conductivity of the electrolyte at higher temperatures [37–39]. The observed higher capacitance at slower scan rates and lower capacitance at higher scan rates suggests that ions have more time to move and accumulate at the electrode-electrolyte interface at lower scan rates [37–39]. Lower scan rates allow ions to penetrate deeper into the porous structure, leading to a larger surface area and forming thicker layers, enhancing the accessible surface area for charge storage and thus increasing capacitance [37–39].

In addition, decreasing the scan rate minimizes the occurrence of polarization effects that arise during the process of charging and discharging [40, 41]. Polarization effects refer to the resistance encountered by ions as they traverse between the electrolyte and electrode surfaces. Reducing polarization enhances the capacity of the charge stored, leading to an augmentation in capacitance [37, 40, 41]. The presence of slight reduction and oxidation edges in lower scan rates for SC-3 is basically due to alkali metals and surface functional groups, that is, oxygenic functionality on rGO surfaces that lead to additional redox processes [37, 40, 41].

Furthermore, the stored physical separation of charges at the electrode-electrolyte interface is combined with a limited amount of pseudocapacitive behavior, in which charge is stored via faradaic redox processes, resulting in minor peaks in the CV data [6, 12, 37]. This suggests the high specific capacitance of SC-3 compared to SC-1 and SC-2 is due to the insertion and intercalation of Na^+ and K^+ ions on the surface of rGO. SC-3 depicted both faradaic and non-faradaic processes; however, the interface between materials is responsible for quick ionic transportation, resulting in higher specific capacitance, and the cathodic and anodic peak shifts represent the slow insertion of dopants [6, 12, 37].

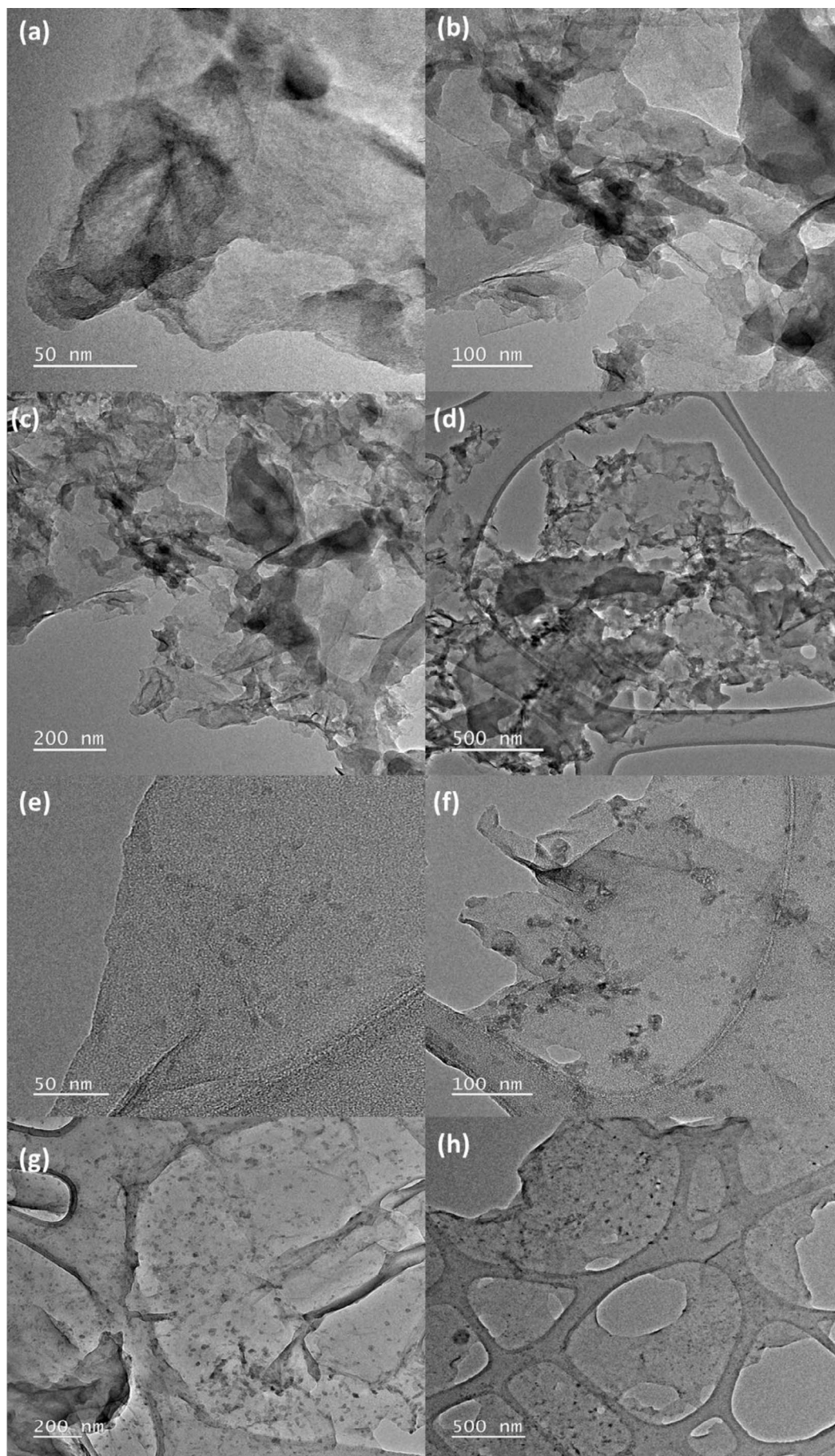


FIGURE 6 | Legend on next page.

FIGURE 6 | TEM images of GO: (a) 50 nm, (b) 100 nm, (c) 200 nm, (d) 500 nm, and TEM images of the composite material; (e) 50 nm, (f) 100 nm, (g) 200 nm, (h) 500 nm.

The total charge storage comprises the faradaic charge involvement caused by alkali metals insertion and the surface ions charge transfer, while the non-faradaic charge involvement is caused by the existence of double-layer behavior [37–39]. Moreover, to examine the impact of the applied potential range on the performance of SC-3, we conducted variable voltage CV at potentials, including 0.5, 1.0, 1.5, and 2 V (Figures 7e–h and S4a). The variable voltage-based stability and reversibility analysis was conducted over 50 cycles each at 50 mV s⁻¹ and 60°C (Figure 7e–h). At a voltage of 0.5 V, the SC-3 exhibited a very precise rectangular form in the CV. As the voltage grew, the shape transformed from a rectangle to an enlarged rectangle at 1 V. At 1.5 V, it exhibited characteristics of both reduction and oxidation halves. When the voltage was raised to 2 V, the SC-3 exhibited a consistent expansion of square shape at higher voltage levels. It demonstrated great stability throughout all cycles and maintained acceptable overlap between cycles across the voltage range.

The peak current seen on the oxidation half side at the 2 V window was higher than that on the reduction half side. This suggests the presence of both faradaic and non-faradaic processes in the composite material. The result shows the better stability and reversibility of SC-3 at 60°C at all voltages, confirming the doping of alkali metals onto the surface of GO. Furthermore, when the temperature rises, the viscosity of [P₄₄₄₄][MEEA] IL reduces, resulting in fast ion diffusivity and many ion contacts at the interface, hence increasing specific capacitance (reported in our previous work) [39].

The Nyquist plots at 60°C indicate that SC-1 exhibits a greater electrode resistance of 123 Ω and electrolyte resistance of 30 Ω, contributing to an overall internal resistance (R_i) of 153 Ω for SC-1. This was higher compared to SC-2, which has a comparatively lower electrode resistance of 72 Ω with charge transfer resistance (R_{ct}) of 20 Ω and a small contribution from Warburg resistance (W) of 2 Ω at lower frequency regions contributing to an overall resistance of 94 Ω for SC-2 (shown in the Randles circuit (Figure 8a–d)).

The SC-2 has a steep slope at the mid-frequency region, with an upright shift in the plot moving farther in the lower-frequency region, indicating its hybrid nature [50]. The evaluations were strengthened by Bode phase plots for SC-1 and SC-2 (Figure S4b,c). These figures demonstrate the frequency response of a system to a phase change represented in degrees using Bode phase graphs. The Bode phase plot for SC-2 shows an S-shaped curve that levels off at high frequencies (−30°) and at low frequencies (90°), whereas SC-1 displays a linear, curvy plot that levels off at high frequencies (0°) and very low frequencies (80°). Greater internal resistance leads to reduced conductivity, resulting in less charge accumulation at the interface in the case of SC-1, which corresponds with the results from CV and confirms the lower capacitance of SC-1 (Figures 8b–d and S4).

The interface interaction was strengthened by the contact angle measurement displayed in the supporting file (Figures S2d and

S4, Table S2). Furthermore, SC-3 displays a resistance contribution from electrode resistance (R_e) of 32 Ω with electrolyte resistance (R_s) of 56 Ω contributing to the overall sheet resistance (R_s) of 88 Ω at a higher frequency region, which shows relatively lower sheet resistance for SC-3, relatively lower than SC-1 and SC-2. This phenomenon demonstrates the combined effect of the electric double-layer creation and charge transfer, as we move from the mid-frequency area to the higher-frequency region [6, 12, 50]. Reducing internal resistance enhances conductivity, which in turn increases the electrically active surface owing to increased charge buildup, leading to the creation of a stable double layer at the interface, resulting in better capacitance and stability for SC-3 evaluations, as well supported by CV [6, 50]. SC-3 offers improved capacitance performance because of the availability of ionic movement, leading to its structural connectivity, which leads to greater surface conductance, a quicker transit time, and an unsaturated electron framework [50–52].

An increase in current generates an electric field that pulls ions from the electrolyte toward the electrode surface, resulting in greater ion accumulation, which increases the effective surface area for storing charge [50–52]. As a result, impedance decreases, allowing more charges to gather on the electrodes, reducing resistance to the flow of electric current, and enhancing capacitance [50–52]. Although decreased electrode thickness, increased ion diffusion, and bulk ion concentration in the electrolyte all affect electrical conductivity and overall device performance in SCs, they are also essential elements in improving performance [53, 54].

Previously, many articles have shown a direct correlation between the electrode materials' surface structure, surface area, pore size, and diameters, with the ion size of electrolyte ions; these factors significantly impact capacitive performance [55, 56].

The galvanic charge–discharge (GCD) tests are performed at the current densities of 0.5, 0.6, 0.7, and 1 A g⁻¹ for SC-1, SC-2, and SC-3 over a potential window of 2 V at 60°C (Figures 8, S3b, and Table S3). SC-1 and SC-2 have consistent IR drops exhibiting higher internal resistance with lower conductivity and surface interaction between the IL electrolyte and electrode surface. The specific capacitance of SC-1 was measured to be 11, 8, 7, and 6 F g⁻¹ at the current densities of 0.5, 0.6, 0.7, and 1 A g⁻¹, respectively. This depicted a continuous decrement in capacitance moving from lower to higher current densities at the potential of 2 V. However, SC-2 does have slightly higher capacitance at similar current densities measured at about 14.5, 12.5, 11.5, and 11 F g⁻¹ at the current densities of 0.5, 0.6, 0.7, and 1 A g⁻¹, respectively (Figure 9a–d). However, a relatively higher specific capacitance was reported for SC-3 compared to SC-2 and SC-1. SC-3 displayed a capacitance of 47, 40, 31, and 25 F g⁻¹, at the current densities of 0.5, 0.6, 0.7, and 1 A g⁻¹, respectively (Figure 9a–d). The discharge time of SC-1, SC-2, and SC-3 shifted to a lower value when moved from 0.5 to 1 A g⁻¹ (Table S3). The discharge time of SC-3 is the

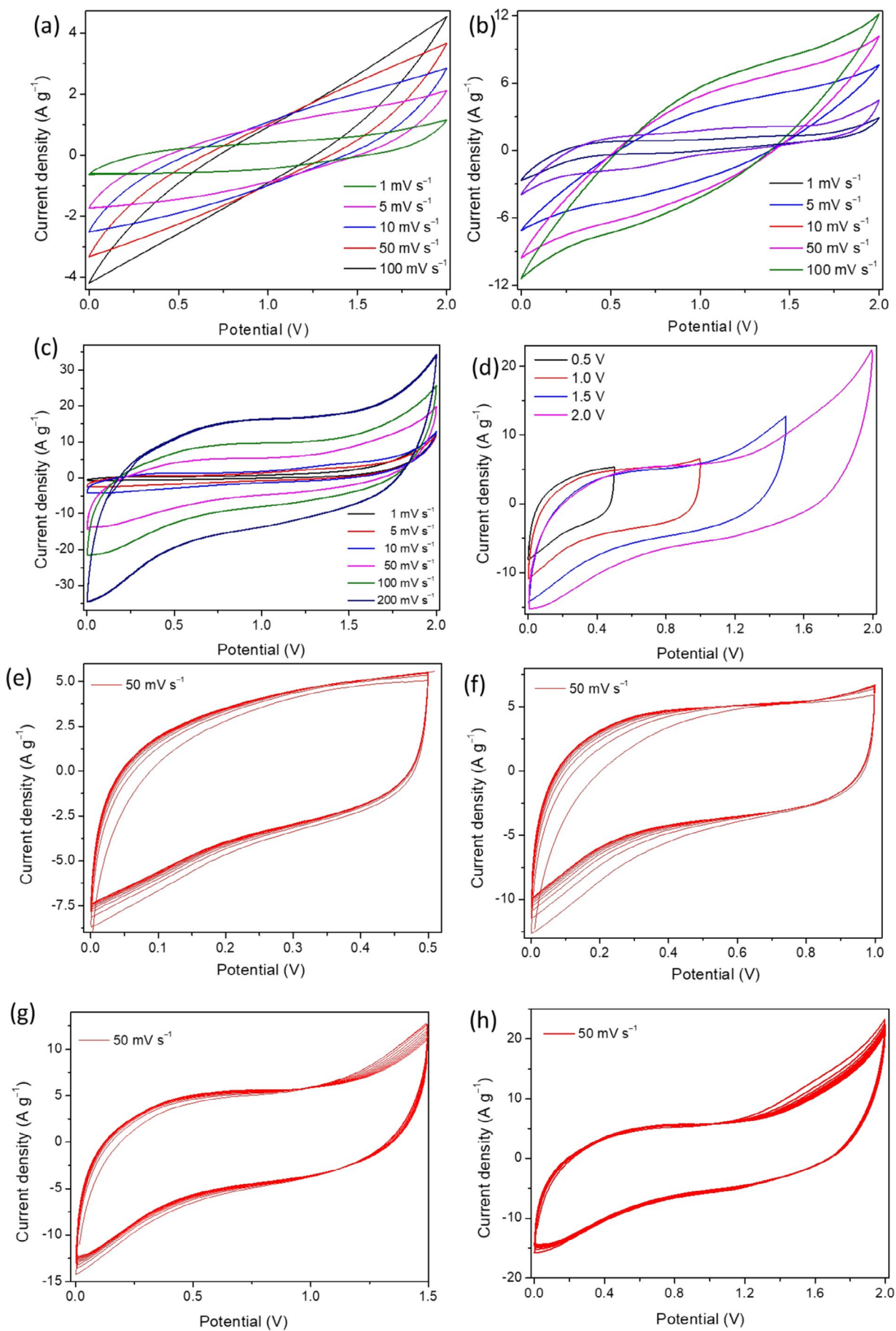


FIGURE 7 | Legend on next page.

FIGURE 7 | CV curves at 60°C using different scan rates: (a) SC-1; (b) SC-2; (c) SC-3; and (d) variable voltage CV for SC-3 at 100 mV s⁻¹. CV curves (50 cycles) for SC-3 at 60°C using a scan rate of 50 mV s⁻¹ for (e) 0.5 V; (f) 1 V; (g) 1.5 V; and (h) 2 V.

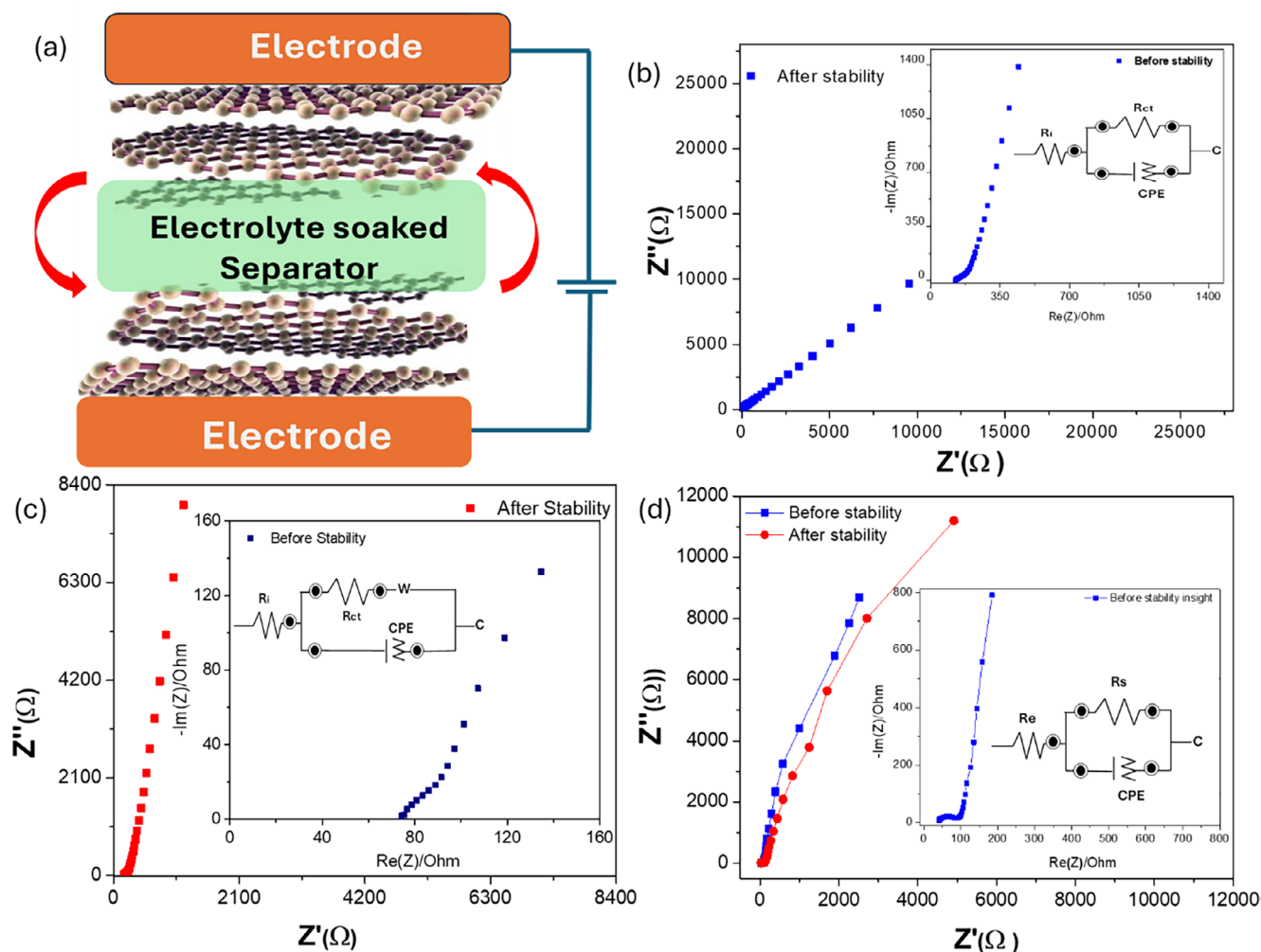


FIGURE 8 | (a) Cell structure of the SCs; and Nyquist plots for (b) SC-1, (c) SC-2, and (d) SC-3.

highest of all, displaying the distorted triangular curve representing the pseudocapacitive discharging. SC-3 showed higher specific capacitance and device performance at the current density of 0.50 A g⁻¹, which slightly decreased with increasing current density to 1 A g⁻¹. The GCD behavior of SC-3 exhibited a notable capacitance and excellent rate capacity, ascribed to the minimal resistance to ion transport and the short distance for diffusion throughout the charging and discharging process. SC-3 had greater capacitance values at lower current densities than SC-2 and SC-1 and showed higher capacitance and stability as the current density increased (Figure S3a–d).

The rate performance of SC-1, SC-2, and SC-3 was systematically evaluated using both CV and GCD measurements, and the results consistently underscored the superiority of SC-3. From CV analysis, SC-3 delivered the highest initial capacitance of 163 F g⁻¹ at 1 mV s⁻¹, substantially higher than SC-2 (119 F g⁻¹) and SC-1 (83 F g⁻¹). More importantly, SC-3 maintained the best retention across increasing scan rates, preserving 89.0%, 58.3%, 42.9%, and 17.2% of its capacitance at 5, 10, 50, and 100 mV s⁻¹, respectively,

compared with 73.9%, 53.8%, 33.6%, and 15.1% for SC-2 and only 57.8%, 34.9%, 15.7%, and 9.6% for SC-1 (Figure S3b).

GCD analysis further reinforced this trend: while all three devices were normalized to 100% retention at 0.5 A g⁻¹, SC-3 retained 85.1% at 0.6 A g⁻¹, higher than SC-1 (73.6%) and comparable to SC-2 (86.2%). At 0.7 A g⁻¹, SC-3 maintained 66.0%, matching SC-1 (66.4%) but demonstrating better stability, and at 1 A g⁻¹, it sustained 53.2%, comparable to SC-1 (54.5%) and only slightly lower than SC-2 (75.9%) (Figure S3d). Although SC-2 exhibited higher retention overall, SC-3 consistently combined higher capacitance values with competitive stability, confirming its superior rate capability across both CV and GCD analyses. The slightly greater decrease in retention for SC-1 and SC-2 as the current density increased can be attributed to their limited charge storage kinetics. Although ionic liquid electrolytes are generally viscous at room temperature, the [P₄₄₄][MEEA] electrolyte employed here exhibits unusually low viscosity, which decreases further at elevated temperature [37–39]. This reduced viscosity enhances electrode

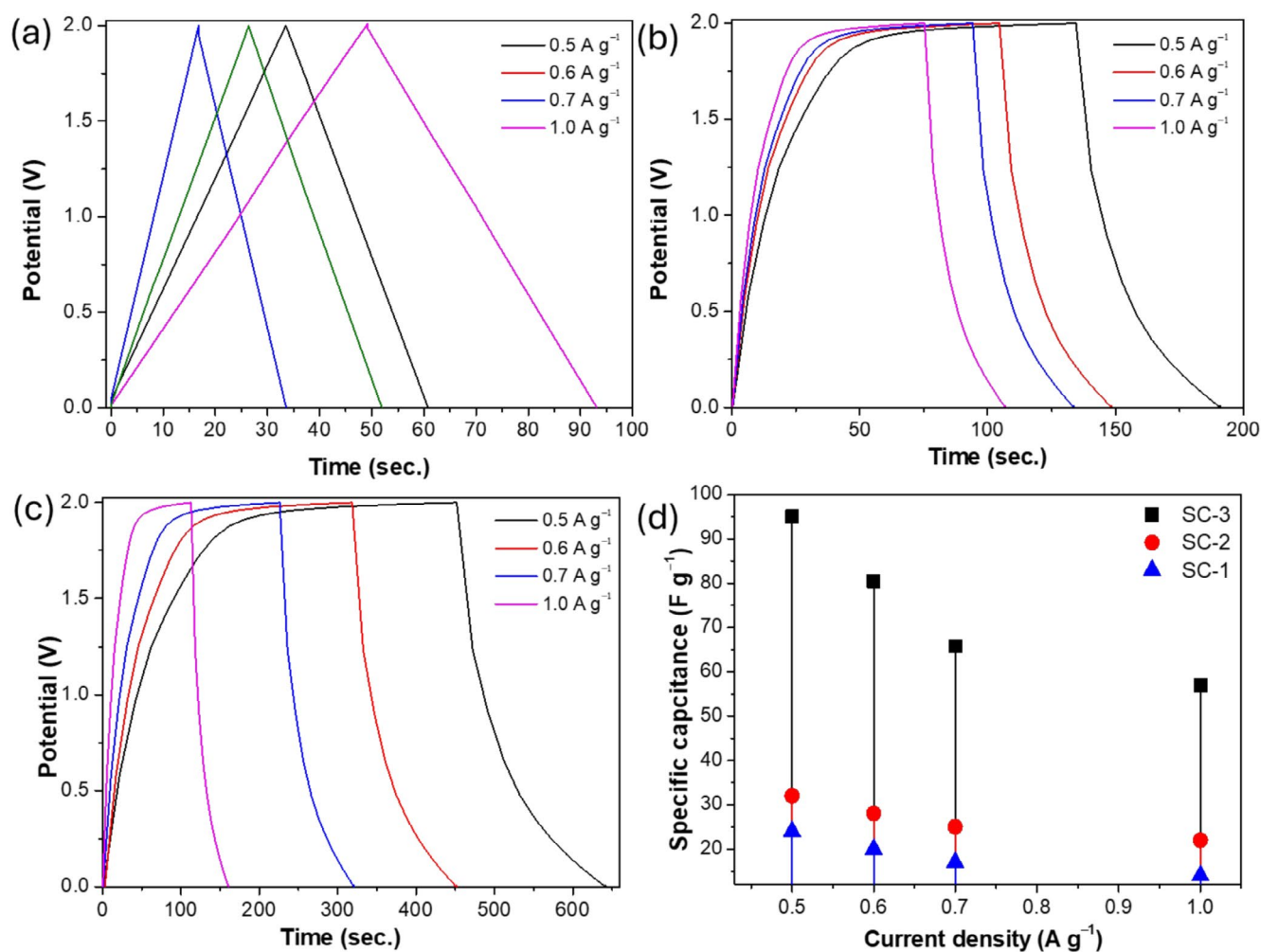


FIGURE 9 | GCD data for (a) SC-1 and (b) SC-2; (c) SC-3; (d) capacitance variation with current density.

pore wetting, while the higher ionic conductivity and faster ion transport promote stable charge–discharge behavior, consistent with the improved capacitance retention observed for SC-3. A comparative examination of scan rate and current density effects (Figure S3a–d) further revealed the expected trend of decreasing capacitance with increasing scan rate or current density across all devices at 60°C.

Beyond capacitance retention, SC-3 also achieved the highest energy densities of 27.77, 23.66, 18.55, and 14.21 Wh kg⁻¹ at current densities of 0.5, 0.6, 0.7, and 1.0 A g⁻¹, respectively, while maintaining corresponding power densities of 500, 597, 652, and 1000 W kg⁻¹ (Figure S3d and Table S4). By contrast, SC-2 delivered significantly lower energy densities of 8.83, 7.50, 6.60, and 6.00 Wh kg⁻¹, while SC-1 showed values of 11.21, 8.10, 7.33, and 6.00 Wh kg⁻¹ at the same current densities, despite both exhibiting identical power densities to SC-3. The similarity in power density across all devices arises from the fixed current and voltage window applied during testing, which yields comparable discharge and thus equalizes the power values.

In contrast, the much higher energy density of SC-3 originates from its substantially larger specific capacitance, enabling greater charge storage within the same voltage window. Taken together, these results demonstrate that SC-3 not only matches

the power-handling capability of the symmetric devices but also delivers significantly enhanced energy storage, making it the most efficient and practical configuration for high-performance supercapacitors.

To assess the long-term cycle stability of SC-1, SC-2, and SC-3, charge–discharge cycling was conducted at 2 A g⁻¹ at 60°C, and the stability of SC-1, SC-2, and SC-3 was tested for 10000 cycles (Figure 10a–c). SC-1 has the lowest efficiency of 79% up to 10000 cycles, while SC-2 has an overall efficiency of 90% up to 10000 cycles, but SC-3 demonstrates extremely good stability with more than 99% coulombic efficiency and exceptional stability (Figure 10d). The superior capacitive performance and long-term charge–discharge stability results of SC-3 can be attributed to its enhanced compatibility between the IL and the asymmetric device structure with rGO on one side and K–Na–GO on the other side, with the IL having lower viscosity and higher ionic conductivity at 60°C [37–39].

The good stability performance of the SCs is attributed to the excellent wetting ability of the [P₄₄₄₄][MEEA] electrolyte, which is critical for maximizing the surface area accessible for charge storage and ensuring efficient ion transport within the device [37–39, 52–54]. While many studies have reported carbon-based composite electrodes for SCs, relatively few have explored the use of fluorine-free ionic liquid electrolytes in combination

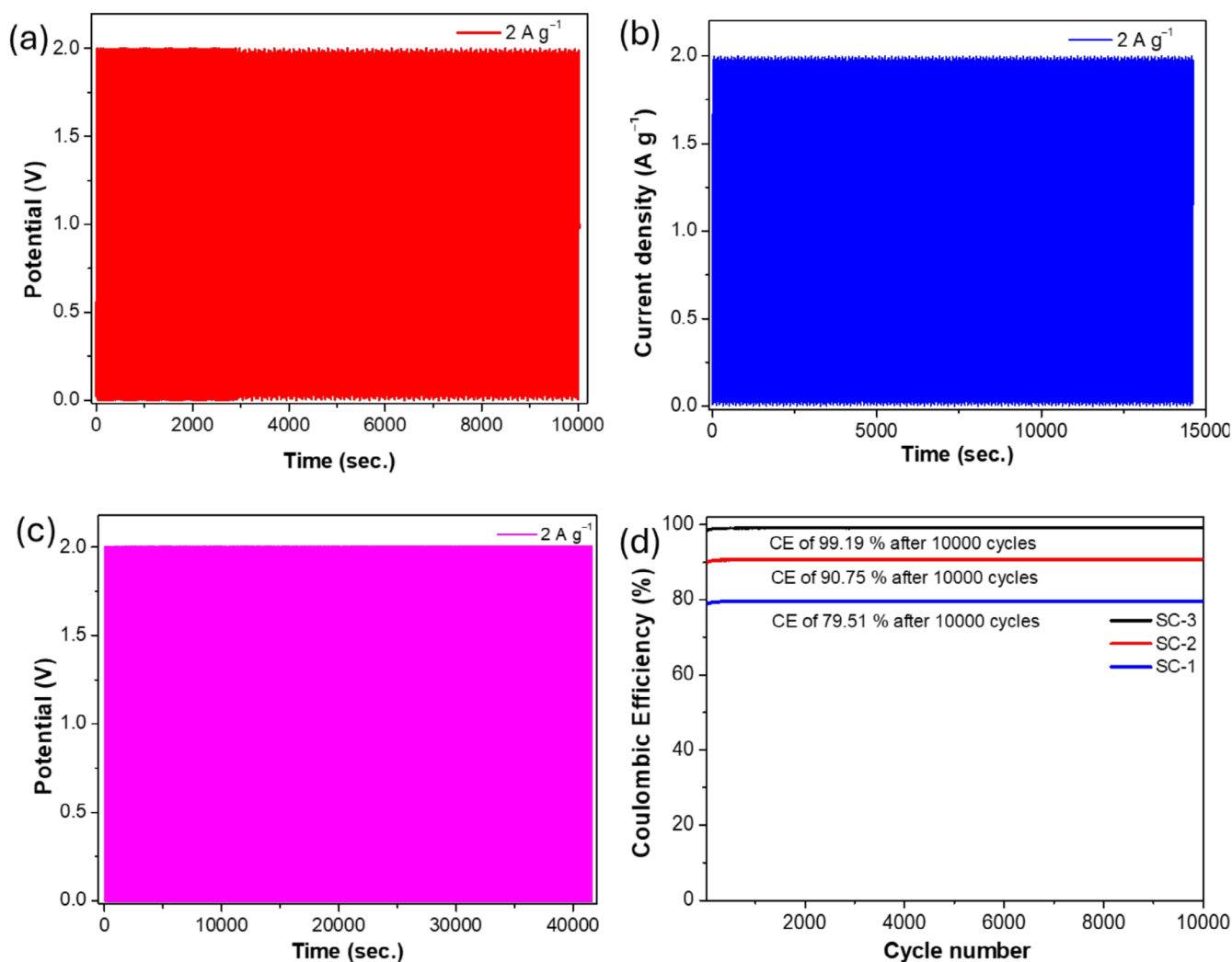


FIGURE 10 | Long-term stability of (a) SC-1, (b) SC-2, (c) SC-3, and (d) CE versus cycle number plot.

with these materials under high-temperature and wide-voltage conditions.

For instance, graphite, coconut husk-derived graphene, MWCNTs, and GO have been employed as electrodes in SCs with fluorine-free ILs, achieving capacitances of 139.7 F g⁻¹ (at 30°C, 5 mV s⁻¹) [12], 88 F g⁻¹ (at 60°C, 5 mV s⁻¹) [32], 164 F g⁻¹ (at 90°C, 1 mV s⁻¹), 138 F g⁻¹ (at 60°C, 1 mV s⁻¹, 2 V window), and 144 F g⁻¹ (at 90°C, 1 mV s⁻¹, 4 V window) [37], respectively. Similarly, microporous carbon paired with an IL electrolyte has been shown to sustain 40,000 stable cycles at 3.5 V and 60°C, owing to the thermal and electrochemical stability of the IL [39]. Collectively, these reports confirm that carbon-based electrodes combined with ILs deliver excellent electrochemical performance in high-temperature SCs with broad voltage ranges. A detailed comparison of electrolyte types and electrode materials (including GO and its composites) in terms of capacitance, energy density, power density, and long-term stability is summarized in Table S5.

The outstanding cycling stability of our devices is closely linked to how their electrode architectures regulate ion transport, interfacial processes, and structural integrity during repeated

operation. In the symmetric SCs, both electrodes operate over nearly identical potential ranges, which minimizes asymmetric stress, suppresses electrolyte decomposition, and ensures highly reversible double-layer charge storage. Co-doping with Na/K further enhances stability by partially restoring graphitic domains for better conductivity, preventing sheet restacking, and maintaining open porosity for efficient ion migration. As a result, SC-2 retained 86.2% of its capacitance at 0.6 A g⁻¹, with an energy density of 8.83 Wh kg⁻¹ at a power density of 500 W kg⁻¹, demonstrating robust cycling stability despite its limited energy output.

In contrast, the asymmetric SC-3 achieves stability through complementary electrode functions: the doped electrode provides high conductivity, reversible ion anchoring, and suppression of side reactions such as hydrogen evolution, while the oxygen-rich GO electrode enhances wettability and ion-buffering capacity, mitigating interfacial degradation. This synergy extends the operating voltage window and stabilizes the electrode–electrolyte interface, allowing SC-3 to deliver 47.01 F g⁻¹ at 0.5 A g⁻¹ and 25.34 F g⁻¹ at 1.0 A g⁻¹, with significantly higher energy densities of 27.77–14.21 Wh kg⁻¹ across the same power density range.

The structural resilience of GO, coupled with the anti-restacking effect of doped-GO, further reduces interface aging and mechanical fatigue, accounting for the near-constant capacitance retention observed over extended cycling. In SC-3, Na⁺ and K⁺ ions play complementary roles in modulating the structural, electronic, and interfacial properties of GO. The simultaneous presence of these alkali ions induces dual ionic polarization within the carbon lattice, promoting partial reduction and restoration of sp²-conjugated domains, as confirmed by XPS and XRD analyses. The smaller Na⁺ ions can intercalate into graphitic interlayers, improving electronic conductivity and facilitating fast charge transfer pathways, while the larger K⁺ ions predominantly adsorb on surface oxygen sites, enhancing electrochemical double-layer capacitance through surface charge accumulation. Furthermore, Na/K incorporation introduces defect-mediated active sites and ionic redox centers associated with Na–O and K–O bonds, which increase the density of accessible charge storage sites. The synergistic effect of lattice reorganization (improved crystallinity and π – π conjugation) and dual-ion surface interaction enhances both pseudocapacitive and double-layer contributions, leading to faster ion diffusion kinetics, reduced charge-transfer resistance, and higher overall capacitance.

4 | Conclusions

The fluorine-free IL electrolyte enabled excellent electrochemical performance of both symmetric and asymmetric SC configurations at elevated temperatures. Among the three fabricated devices, two symmetric (SC-1 and SC-2) and one asymmetric (SC-3), the symmetric systems exhibited considerably lower capacitance compared to the asymmetric device. While SC-2 maintained stable capacitance retention as a symmetric device, SC-3 distinctly outperformed both symmetric systems by achieving higher capacitance and superior rate capability, highlighting its clear advantage as the most efficient configuration.

In the asymmetric device, Na⁺ and K⁺ ions play complementary roles in modulating the structural, electronic, and interfacial properties of GO. The coexistence of both alkali ions induces dual ionic polarization within the carbon framework, promoting partial reduction and restoration of sp²-conjugated domains, as supported by XPS and XRD analyses. The smaller Na⁺ ions intercalate between graphitic layers to enhance electronic conductivity and charge transport, whereas the larger K⁺ ions adsorb on the surfaces, improving electrochemical double-layer capacitance through surface charge accumulation. Additionally, the formation of Na–O and K–O coordination sites introduces defect-mediated active centers, increasing the density of accessible charge storage sites.

The fluorine-free IL [P₄₄₄₄][MEEA] further contributes to superior electrochemical performance by providing a wide potential window, high ionic conductivity, and thermal stability, ensuring efficient ion transport and robust electrode–electrolyte interactions. Among all the fabricated devices, SC-3 exhibited the highest specific capacitance (47.01 Fg^{−1}), energy density (27.77 Wh kg^{−1} at 0.5 A g^{−1}), and power density (1000 W kg^{−1} at 1 A g^{−1}), along with excellent cycling stability (99% retention after 10 000 cycles at 60°C).

The synergistic Na–K co-doping and fluorine-free IL electrolyte enhance structural order, charge transport, and interfacial stability, yielding superior conductivity and charge storage. Thus, the Na–K co-doped rGO electrodes in combination with the fluorine-free IL offer a sustainable and efficient platform for higher temperature symmetric and asymmetric supercapacitors.

Author Contributions

Gaurav Tatrari: conceptualization, investigation, formal analysis, validation, and original draft. Tanmoy Rath: formal analysis. Klaudia Maślana: XRD, XPS, SEM, and TEM characterization, supporting investigations. Rajesh Bhatt: GO synthesis at Prof. Nanda Gopal Sahoo's laboratory (PRS-Nanoscience and Nanotechnology Centre, Kumaun University, Nainital, India). Xuecheng Chen: review and editing; Ewa Mijowska: review and editing; Rong An: contact angle measurements, and editing. Solomon Tesfalidet: review and editing. Faiz Ullah Shah: supervision, validation, review, and editing.

Acknowledgments

The Kempe Foundation, in the memory of J. C. and Seth M. Kempe, is gratefully acknowledged for the financial assistance for G.T. (grant numbers JCK22-0045 and JCSMK023-0170 and the equipment grant number: JCSMK23-0090). The synthesis of GO was performed at Prof. Nanda Gopal Sahoo's laboratory, PRS-Nanoscience and Nanotechnology Centre, Department of Chemistry, D.S.B. Campus, Kumaun University, Nainital, Uttarakhand, India, and is gratefully acknowledged.

Funding

This work was supported by Kempe Foundation, JCK22-0045, JCSMK023-0170, CSMK23-0090.

Conflicts of Interest

The authors declare no conflicts of interest.

Data Availability Statement

The data that supports the findings of this study are available in Appendix S1 of this article.

References

1. G. Tatrari, R. An, and F. U. Shah, "Designed Metal-Organic Framework Composites for Metal-Ion Batteries and Metal-Ion Capacitors," *Coordination Chemistry Reviews* 512 (2024): 215876.
2. G. Tatrari, M. Ahmed, and F. U. Shah, "Synthesis, Thermoelectric and Energy Storage Performance of Transition Metal Oxides Composites," *Coordination Chemistry Reviews* 498 (2024): 215470.
3. P. Simon, Y. Gogotsi, and B. Dunn, "Where Do Batteries End and Supercapacitors Begin?," *Science* 343, no. 6176 (2014): 1210–1211.
4. G. Tatrari, M. Karakoti, C. Tewari, et al., "Solid Waste-Derived Carbon Nanomaterials for Supercapacitor Applications: A Recent Overview," *Materials Advances* 2, no. 5 (2021): 1454–1484.
5. W. Zuo, R. Li, C. Zhou, Y. Li, J. Xia, and J. Liu, "Battery-Supercapacitor Hybrid Devices: Recent Progress and Future Prospects," *Advanced Science* 4, no. 7 (2017): 1600539.
6. G. Tatrari, C. Tewari, M. Pathak, et al., "3D-Graphene Hydrogel and Tungsten Trioxide-MnO₂ Composite for Ultra-High-Capacity Asymmetric Supercapacitors: A Comparative Study," *Journal of Energy Storage* 68 (2023): 107830.

7. J. Gao, S. Tian, L. Qi, M. Yoshio, and H. Wang, "Hexafluorophosphate Intercalation Into Graphite Electrode From Gamma-Butyrolactone Solutions in Activated Carbon/Graphite Capacitors," *Journal of Power Sources* 297 (2015): 121–126.
8. G. Yang, L. Li, W. B. Lee, and M. C. Ng, "Structure of Graphene and Its Disorders: A Review," *Science and Technology of Advanced Materials* 19, no. 1 (2018): 613–648.
9. N. G. Sahoo, "Quantum Dots Based Materials for New Generation Supercapacitors Application: A Recent Overview," *Materials Research Foundations* 96 (2021): 215.
10. G. Tatrari, C. Tewari, M. Pathak, et al., "Bulk Production of Zinc Doped Reduced Graphene Oxide From Tire Waste for Supercapacitor Application: Computation and Experimental Analysis," *Journal of Energy Storage* 53 (2022): 105098.
11. D. G. Papageorgiou, I. A. Kinloch, and R. J. Young, "Mechanical Properties of Graphene and Graphene-Based Nanocomposites," *Progress in Materials Science* 90 (2017): 75–127.
12. N. Sahoo, G. Tatrari, C. Tewari, M. Karakoti, B. S. Bohra, and A. Danadapat, "Vanadium Pentoxide-Doped Waste Plastic-Derived Graphene Nanocomposite for Supercapacitors: A Comparative Electrochemical Study of Low and High Metal Oxide Doping," *RSC Advances* 12, no. 9 (2022): 5118–5134.
13. G. Tatrari, C. Tewari, M. Pathak, et al., "Coconut-Husk Derived Graphene for Supercapacitor Applications: Comparative Analysis of Polymer Gel and Aqueous Electrolytes," *Materials Advances* 4, no. 15 (2023): 3310–3322.
14. C. Li, C. Zheng, F. Cao, Y. Zhang, and X. Xia, "The Development Trend of Graphene Derivatives," *Journal of Electronic Materials* 51, no. 8 (2022): 4107–4114.
15. D. Chen, H. Feng, and J. Li, "Graphene Oxide: Preparation, Functionalization, and Electrochemical Applications," *Chemical Reviews* 112, no. 11 (2012): 6027–6053.
16. A. T. Dideikin and A. Y. Vul', "Graphene Oxide and Derivatives: The Place in Graphene Family," *Frontiers in Physics* 6 (2019): 149.
17. N. S. Suhaimin, M. F. R. Hanifah, M. Azhar, et al., "The Evolution of Oxygen-Functional Groups of Graphene Oxide as a Function of Oxidation Degree," *Materials Chemistry and Physics* 278 (2022): 125629.
18. T. Van Khai, H. G. Na, D. S. Kwak, et al., "Comparison Study of Structural and Optical Properties of Boron-Doped and Undoped Graphene Oxide Films," *Chemical Engineering Journal* 211 (2012): 369–377.
19. A. Cai, H. He, Q. Zhang, et al., "Synergistic Effect of N-Doped sp² Carbon and Porous Structure in Graphene Gels Toward Selective Oxidation of C–H Bond," *ACS Applied Materials & Interfaces* 13, no. 11 (2021): 13087–13096.
20. K. C. Kwon, K. S. Choi, C. Kim, and S. Y. Kim, "Role of Metal Cations in Alkali Metal Chloride Doped Graphene," *Journal of Physical Chemistry C* 118, no. 15 (2014): 8187–8193.
21. S. Naghdi, H. Y. Song, A. Várez, K. Y. Rhee, and S. W. Kim, "Engineering the Electrical and Optical Properties of Graphene Oxide via Simultaneous Alkali Metal Doping and Thermal Annealing," *Journal of Materials Research and Technology* 9, no. 6 (2020): 15824–15837.
22. T. Hussain, M. Hankel, and D. J. Searles, "Graphenylene Monolayers Doped With Alkali or Alkaline Earth Metals: Promising Materials for Clean Energy Storage," *Journal of Physical Chemistry C* 121, no. 27 (2017): 14393–14400.
23. L. Xia, B. Tang, J. Wei, and Z. Zhou, "Recent Advances in Alkali Metal-Ion Hybrid Supercapacitors," *Batteries & Supercaps* 4, no. 7 (2021): 1108–1121.
24. G. Tatrari, C. Tewari, M. Karakoti, et al., "Mass Production of Metal-Doped Graphene From the Agriculture Waste of *Quercus Ilex* Leaves for Supercapacitors: Inclusive DFT Study," *RSC Advances* 11, no. 18 (2021): 10891–10901.
25. L. Niu, Z. Li, W. Hong, et al., "Pyrolytic Synthesis of Boron-Doped Graphene and Its Application as Electrode Material for Supercapacitors," *Electrochimica Acta* 108 (2013): 666–673.
26. G. B. Appetecchi, F. Croce, L. Persi, F. Ronci, and B. Scrosati, "Transport and Interfacial Properties of Composite Polymer Electrolytes," *Electrochimica Acta* 45, no. 8–9 (2000): 1481–1490.
27. F. Wu, K. Zhang, Y. Liu, et al., "Polymer Electrolytes and Interfaces Toward Solid-State Batteries: Recent Advances and Prospects," *Energy Storage Materials* 33 (2020): 26–54.
28. D. T. Hallinan, Jr. and N. P. Balsara, "Polymer Electrolytes," *Annual Review of Materials Research* 43, no. 1 (2013): 503–525.
29. I. A. Khan, O. I. Gnezdilov, Y. L. Wang, A. Filippov, and F. U. Shah, "Effect of Aromaticity in Anion on the Cation–Anion Interactions and Ionic Mobility in Fluorine-Free Ionic Liquids," *Journal of Physical Chemistry B* 124, no. 52 (2020): 11962–11973.
30. H. Liu and H. Yu, "Ionic Liquids for Electrochemical Energy Storage Devices Applications," *Journal of Materials Science and Technology* 35, no. 4 (2019): 674–686.
31. S. Bhowmick, A. Filippov, I. A. Khan, and F. U. Shah, "Physical and Electrochemical Properties of New Structurally Flexible Imidazolium Phosphate Ionic Liquids," *Physical Chemistry Chemical Physics* 24, no. 38 (2022): 23289–23300.
32. I. A. Khan, Y. L. Wang, and F. U. Shah, "Effect of Structural Variation in Biomass-Derived Nonfluorinated Ionic Liquids Electrolytes on the Performance of Supercapacitors," *Journal of Energy Chemistry* 69 (2022): 174–184.
33. I. A. Khan, O. I. Gnezdilov, A. Filippov, and F. U. Shah, "Ion Transport and Electrochemical Properties of Fluorine-Free Lithium-Ion Battery Electrolytes Derived From Biomass," *ACS Sustainable Chemistry & Engineering* 9, no. 23 (2021): 7769–7780.
34. F. U. Shah, S. Glavatskih, P. M. Dean, D. R. MacFarlane, M. Forsyth, and O. N. Antzutkin, "Halogen-Free Chelated Orthoborate Ionic Liquids and Organic Ionic Plastic Crystals," *Journal of Materials Chemistry* 22, no. 14 (2012): 6928–6938.
35. F. U. Shah, S. Glavatskih, D. R. MacFarlane, A. Somers, M. Forsyth, and O. N. Antzutkin, "Novel Halogen-Free Chelated Orthoborate–Phosphonium Ionic Liquids: Synthesis and Tribophysical Properties," *Physical Chemistry Chemical Physics* 13, no. 28 (2011): 12865–12873.
36. A. Filippov, N. Azancheev, M. Taher, et al., "Self-Diffusion and Interactions in Mixtures of Imidazolium Bis (Mandelato) Borate Ionic Liquids With Polyethylene Glycol: 1H NMR Study," *Magnetic Resonance in Chemistry* 53, no. 7 (2015): 493–497.
37. G. Tatrari, S. Bhowmick, A. Filippov, R. An, and F. U. Shah, "Charge Storage Performance of a Structurally Flexible Hybrid Ionic Liquid Electrolyte," *Energy Storage* 6, no. 1 (2024): e535.
38. S. Bhowmick, G. Tatrari, A. Filippov, P. Johansson, and F. U. Shah, "Structurally Flexible Pyrrolidinium- and Morpholinium-Based Ionic Liquid Electrolytes," *Physical Chemistry Chemical Physics* 25, no. 29 (2023): 19815–19823.
39. F. U. Shah, O. I. Gnezdilov, I. A. Khan, A. Filippov, N. A. Slad, and P. Johansson, "Structural and Ion Dynamics in Fluorine-Free Oligoether Carboxylate Ionic Liquid-Based Electrolytes," *Journal of Physical Chemistry B* 124, no. 43 (2020): 9690–9700.
40. G. Tatrari, M. Pathak, D. Bhatt, K. Garwal, F. U. Shah, and N. G. Sahoo, "Electrochemistry and Energy Storage Applications of Graphene and Its Derivatives," in *Electrochemical Exfoliation of Graphene and Its Derivatives: Commercial Applications* (Springer Nature Singapore, 2024), 217–239.

41. E. Paek, A. J. Pak, and G. S. Hwang, "On the Influence of Polarization Effects in Predicting the Interfacial Structure and Capacitance of Graphene-Like Electrodes in Ionic Liquids," *Journal of Chemical Physics* 142, no. 2 (2015): 24701.
42. H. Yang, H. Hu, Z. Ni, et al., "Comparison of Surface-Enhanced Raman Scattering on Graphene Oxide, Reduced Graphene Oxide and Graphene Surfaces," *Carbon* 62 (2013): 422–429.
43. G. Surekha, K. V. Krishnaiah, N. Ravi, and R. P. Suvarna, "FTIR, Raman and XRD Analysis of Graphene Oxide Films Prepared by Modified Hummers Method," *Journal of Physics: Conference Series* 1495, no. 1 (2020): 12012.
44. L. Shahriary and A. A. Athawale, "Graphene Oxide Synthesized by Using Modified Hummers Approach," *International Journal of Renewable Energy Environment Engineering* 2, no. 1 (2014): 58–63.
45. C. Tewari, M. Pathak, G. Tatrari, et al., "Waste Plastics Derived Reduced Graphene Oxide-Based Nanocomposite With Fe₃O₄ for Water Purification and Supercapacitor Applications," *Journal of Industrial and Engineering Chemistry* 130 (2024): 346–356.
46. M. Karakoti, S. Pandey, G. Tatrari, et al., "A Waste to Energy Approach for the Effective Conversion of Solid Waste Plastics Into Graphene Nanosheets Using Different Catalysts for High Performance Supercapacitors: A Comparative Study," *Materials Advances* 3, no. 4 (2022): 2146–2157.
47. Y. C. G. Kwan, G. M. Ng, and C. H. A. Huan, "Identification of Functional Groups and Determination of Carboxyl Formation Temperature in Graphene Oxide Using the XPS O 1s Spectrum," *Thin Solid Films* 590 (2015): 40–48.
48. R. Al-Gaashani, A. Najjar, Y. Zakaria, S. Mansour, and M. A. Atieh, "XPS and Structural Studies of High Quality Graphene Oxide and Reduced Graphene Oxide Prepared by Different Chemical Oxidation Methods," *Ceramics International* 45, no. 11 (2019): 14439–14448.
49. Y. H. Lee, K. H. Chang, and C. C. Hu, "Differentiate the Pseudocapacitance and Double-Layer Capacitance Contributions for Nitrogen-Doped Reduced Graphene Oxide in Acidic and Alkaline Electrolytes," *Journal of Power Sources* 227 (2013): 300–308.
50. B. A. Mei, O. Munteshari, J. Lau, B. Dunn, and L. Pilon, "Physical Interpretations of Nyquist Plots for EDLC Electrodes and Devices," *Journal of Physical Chemistry C* 122, no. 1 (2018): 194–206.
51. A. Ghosh and Y. H. Lee, "Carbon-Based Electrochemical Capacitors," *ChemSusChem* 5, no. 3 (2012): 480–499.
52. L. Wang, J. Zhao, X. He, et al., "Electrochemical Impedance Spectroscopy (EIS) Study of LiNi_{1/3}Co_{1/3}Mn_{1/3}O₂ for Li-Ion Batteries," *International Journal of Electrochemical Science* 7, no. 1 (2012): 345–353.
53. B. Y. Chang and S. M. Park, "Electrochemical Impedance Spectroscopy," *Annual Review of Analytical Chemistry* 3, no. 1 (2010): 207–229.
54. S. Bhakta, G. Tatrari, M. Rudakova, A. Filippov, and F. U. Shah, "Fluorine-Free Biomass-Derived Ionic Liquid Electrolytes: Ion Dynamics and Electrochemical Properties," *Chemistry—a European Journal* 31 (2025): e01641.
55. M. Ahmed, G. Tatrari, P. Johansson, and F. U. Shah, "Sweet Ionic Liquids as High-Temperature and High-Voltage Supercapacitor Electrolytes," *ACS Sustainable Chemistry & Engineering* 12, no. 46 (2024): 16896–16904.
56. M. Saha, A. Kumar, R. Kanaoujiya, K. Behera, and S. Trivedi, "A Comprehensive Review of Novel Emerging Electrolytes for Supercapacitors: Aqueous and Organic Electrolytes Versus Ionic Liquid-Based Electrolytes," *Energy & Fuels* 38, no. 10 (2024): 8528–8552.

Supporting Information

Additional supporting information can be found online in the Supporting Information section. **APPENDIX S1:** Supporting information.